Relaxation by thermal conduction of a magnetically confined mountain on an accreting neutron star

A.G. Suvorov^{1*}, A. Melatos^{1,2}
¹ School of Physics, University of Melbourne, Parkville VIC 3010, Australia

- ² Australian Research Council Centre of Excellence for Gravitational Wave Discovery (OzGrav)

Accepted ?. Received ?; in original form ?

ABSTRACT

A magnetically confined mountain on the surface of an accreting neutron star simultaneously reduces the global magnetic dipole moment through magnetic burial and generates a mass quadrupole moment, which emits gravitational radiation. Previous mountain models have been calculated for idealized isothermal and adiabatic equations of state. Here these models are generalised to include non-zero, finite thermal conduction. Grad-Shafranov equilibria for three representative, polytropic equations of state are evolved over many conduction time-scales with the magnetohydrodynamic solver PLUTO. It is shown that conduction facilitates the flow of matter towards the pole. Consequently the buried magnetic field is partially resurrected starting from an initially polytropic Grad-Shafranov equilibrium. The poleward mass current makes the star more prolate, marginally increasing its detectability as a gravitational wave source, though to an extent which is likely to be subordinate to other mountain physics. Thermal currents also generate filamentary hot spots ($\gtrsim 10^8$ K) in the mountain, especially near the pole where the heat flux is largest, with implications for type I X-ray bursts.

Key words: stars: neutron, accretion, magnetic fields, gravitational waves

INTRODUCTION

Observations of binary neutron stars with white dwarf or supergiant companions and a history of accretion suggest that the neutron star magnetic dipole moment μ decreases over time, as the accreted mass M_a increases (Taam & van den Heuvel 1986; van den Heuvel & Bitzaraki 1995; Zhang & Kojima 2006; Patruno 2012). Several theoretical mechanisms exist to explain the trend, such as accelerated Ohmic decay (Urpin & Geppert 1995), interactions between superfluid vortices and superconductor flux tubes within the stellar interior (Srinivasan et al. 1990), or the process of magnetic burial (Blondin & Freese 1986; Shibazaki et al. 1989). In magnetic burial, the focus of this paper, matter is guided onto the polar cap by the magnetic field to form a mountain-like density profile supported by the compressed equatorial magnetic field ('magnetic mountain') (Brown & Bildsten 1998; Melatos & Phinney 2001; Payne & Melatos 2004; Mukherjee & Bhattacharya 2012; Wang et al. 2012). The resulting mass quadrupole moment emits gravitational radiation (Ushomirsky et al. 2000; Melatos & Payne 2005; Vigelius & Melatos 2009c; Priymak et al. 2011; Lasky 2015).

The short-term stability and long-term relaxation of a magnetic mountain have been studied by several authors. In the short term, on the Alfvén and tearing-mode time-scales, axisymmetric mountain equilibria are susceptible to the undular submode of the Parker instability (Payne & Melatos 2006a; Vigelius & Melatos 2008, 2009a) and to pressuredriven toroidal-mode instabilities (Cumming et al. 2001; Litwin et al. 2001; Mukherjee et al. 2013a,b), once M_a exceeds a critical threshold. The system is not necessarily disrupted; the instability saturates, and the mountain adjusts to a new equilibrium, stabilized by magnetic line-tying at the stellar surface and the compressed magnetic 'wall' at the equator (Vigelius & Melatos 2008). In the long term, the mountain relaxes due to Ohmic dissipation (Vigelius & Melatos 2009b), soft-crust sinking (Wette et al. 2010), or a combination of the latter two processes (Konar & Choudhuri 2002, 2004; Konar 2010). Its structure is modified also by factors like the Hall effect (Cumming 2004; Geppert & Viganò 2014) and the equation of state (EOS) (Priymak et al. 2011).

Mountains on recycled pulsars may be responsible for

the discrepancy between magnetic field strengths inferred from spin-down and cyclotron line measurements (Arons 1993; Nishimura 2005). The local magnetic field can be $\sim 10^4$ times stronger than the global value inferred from μ (Mastrano & Melatos 2012; Mukherjee & Bhattacharya 2012). Once M_a increases beyond a certain level, phasedependent cyclotron resonance scattering features are predicted to emerge in the X-ray spectrum (Priymak et al. 2014). Additionally, X-ray observations of neutron star binaries reveal type I X-ray bursts with recurrence times ranging between a few minutes and $\sim 10^3$ hours (Galloway et al. 2008). Recurrence times $\lesssim 10 \text{ min (e.g. in 4U } 1608-522)$ are too short for many theoretical ignition models and may indicate the existence of multiple, isolated patches of fuel on the stellar surface (Bhattacharyya & Strohmayer 2006), which are fenced-off magnetically if the polar magnetic field geometry is complicated (Payne & Melatos 2006b; Keek et al. 2010; Misanovic et al. 2010). A simultaneous detection of gravitational waves, X-ray bursts with short recurrence times, and cyclotron features in an X-ray binary some time in the future would strongly indicate the presence of a magnetic mountain (Haskell et al. 2015).

In this paper we include thermal conduction in magnetic mountain models self-consistently for the first time. Thermal conduction is potentially important, because the mountain forms at an elevated temperature, caused by accretiondriven heating, and cools through its sides (if accretion is confined to a narrow column) or throughout its volume (once accretion switches off). Thermal fluxes directed out of localized polar hot spots control the instantaneous hydromagnetic structure of the mountain by regulating the EOS (Priymak et al. 2011) and the long-term, quasistatic relaxation of the mountain by regulating temperature-sensitive dissipative mechanisms like Ohmic decay (Vigelius & Melatos 2009b). Modeling thermal conduction in magnetic mountains self-consistently is therefore important for understanding the relationship between hot spots, magnetic fields, Xray burst activity, and gravitational radiation, providing the basis for multi-messenger tests of the polar magnetic burial scenario.

The purpose of this paper is to elucidate, with the aid of numerical simulations, the dominant thermal processes that modify the short-term structure and long-term evolution of a magnetic mountain, when thermal conduction is "switched on" in the model. Predictions are made, in broad qualitative terms, regarding how potentially observable properties (e.g. μ) are affected by thermal conduction. We emphasize, however, that the simulations are not yet at the point where they yield highly realistic mountain models, which are ready to be compared in detail with observational data. Such comparisons would require a more sophisticated description of the stratified structure, composition, and EOS of the crust, better observational knowledge of the high-order magnetic multipoles near the surface, and expanded computational resources to handle the disparate thermal and hydromagnetic time-scales in the problem. Our investigation proceeds in two stages. In Section 2, we use the Grad-Shafranov solver developed by Payne & Melatos (2004) and extended by Privmak et al. (2011) to calculate the steady-state structure given an EOS and an initially dipolar magnetic field. We then numerically evolve the Grad-Shafranov equilibrium using the magnetohydrodynamics (MHD) code PLUTO (Mignone et al. 2007) with and without thermal conduction in Sections 3 (set-up details and local mountain properties) and 4 (global observables) and compare the effects on potentially observable properties such as μ . Long-term thermal relaxation is explored in Section 5. Finally, the astrophysical implications of the results, including for gravitational wave emission, are discussed briefly in Section 6.

2 POLAR MAGNETIC BURIAL

2.1 Qualitative behaviour

During accretion, the neutron star's polar magnetic field buckles underneath the infalling matter, and the field lines spread equatorially due to flux freezing. The lateral pressure gradient at the base of the accreted mountain is balanced by the Lorentz force in the compressed, equatorial magnetic belt. This process is illustrated schematically in Figure 1 [see also Figure 6 of Priymak et al. (2011)]. The compressed magnetic field is more intense than the pre-accretion field locally, due to magnetic flux conservation, but the global moment μ reduces, because the magnetic distortion induces screening currents, which reduce the radial magnetic field near the pole (Vigelius & Melatos 2008; Mastrano & Melatos 2012).

It is observed that μ decreases with M_a in binary systems (Taam & van den Heuvel 1986; van den Heuvel & Bitzaraki 1995; Zhang & Kojima 2006). Shibazaki et al. (1989) proposed the widely used, empirical law

$$\mu = \mu_i \left(1 + M_a / M_c \right)^{-1}. \tag{1}$$

In (1), we define M_c to be the critical accreted mass, for which the global dipole moment is halved. The dipole moment before accretion begins is given by $\mu_i = B_{\star} R_{\star}^3$. We take $R_{\star} = 10^6$ cm for the stellar radius and $B_{\star} = 10^{12.5}$ G for the natal magnetic field strength at the polar surface, in line with population synthesis models (Arzoumanian et al. 2002; Faucher-Giguère & Kaspi 2006). Self-consistent, MHD simulations reproduce the empirical scaling (1) for small accreted masses $M_a \ll M_c$ in isothermal and adiabatic mountains with $M_c\sim 10^{-6}M_\odot$ and $M_c\sim 10^{-8}M_\odot$ respectively (Payne & Melatos 2004; Vigelius & Melatos 2009a; Priymak et al. 2011). For $10^{-1} \lesssim M_a/M_c \lesssim 10$, the simple estimate in (1) breaks down and the burial effect is better represented by a power-law $\mu/\mu_i = (M_a/M_c)^{-a}$, where $1 \leqslant a \leqslant 2.47$ depends on the EOS [see section 4.1 of Priymak et al. (2011) and Fig. 8(c) of Payne & Melatos (2004)]. Numerical difficulties prevent simulations from probing the regime $M_a/M_c \gtrsim 10$, where a significant deviation from (1) is expected (Haskell et al. 2015), though Ohmic diffusion sets a burial limit of $\mu/\mu_i \gtrsim 10^{-8}$ (Vigelius & Melatos 2009b).

The critical mass M_c depends strongly on the EOS (Priymak et al. 2011). For a softer EOS, the mountain has a relatively small thickness ($H_{\rm max} \sim 10^3$ cm), because the material is easier to compress. Strong local magnetic fields ($\lesssim 10^{15}$ G) exist near the stellar surface, as polar field lines buckle, and the polar magnetic flux is squeezed into a small volume. Consequently, the screening currents flow closer to the stellar surface for a softer EOS than for a harder EOS, and μ reduces less for a given M_a . For a softer EOS, the critical mass is found to lie in the range $10^{-5} \lesssim M_c/M_{\star} \lesssim 10^{-2}$ (Payne & Melatos 2004). For a harder EOS, the mountain is

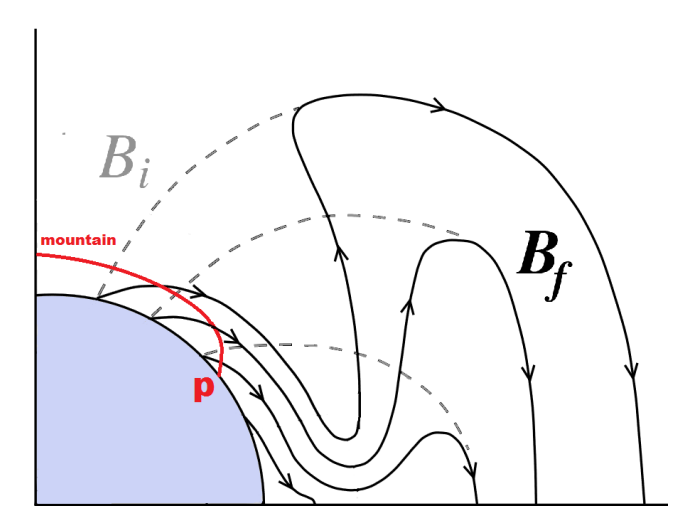


Figure 1. Schematic diagram (not to scale) of the magnetic field lines prior to (dashed curves) and after (solid curves) accretion. The shaded region represents the neutron star. The mountain fills the region bounded between the red curve and the stellar surface. The pressure gradient at the base of the mountain is balanced by the Lorentz force in the compressed, equatorial magnetic belt. The edge of the mountain (point p) moves towards the equator, as M_a increases. [Adapted from Melatos & Phinney (2001).]

thicker ($H_{\rm max} \sim 10^4$ cm), and μ reduces further. For a polytropic EOS with index $\Gamma \gtrsim 4/3$, the critical mass is found to lie in the range $10^{-9} \lesssim M_c/M_\star \lesssim 10^{-6}$ (Priymak et al. 2011). Priymak et al. (2011) found $M_c \propto B_\star^2$.

The mountain mass quadrupole moment can be expressed in terms of the mass ellipticity ϵ , which is given approximately by (Melatos & Payne 2005)

$$\epsilon \approx (5M_a/4M_{\star})(1 + 9M_a/8M_c)^{-1},$$
 (2)

where $M_{\star}=1.4M_{\odot}$ is the stellar mass. Therefore, for a given accreted mass, there is a one-to-one relationship between μ and ϵ through (1) and (2) which depends on the value of M_c . The mass quadrupole moment emits gravitational radiation, as the star spins (Melatos & Payne 2005). The implications are discussed in Section 4.2.

2.2 Hydromagnetic equilibrium

The hydromagnetic structure of the mountain has been calculated for various EOS previously (Payne & Melatos 2004, 2006a; Vigelius & Melatos 2008; Priymak et al. 2011; Mukherjee et al. 2013a). In this paper, we start by solving for the structure of a steady-state $(\partial/\partial t=0)$ and immobile $(\boldsymbol{v}=0)$, where \boldsymbol{v} is the fluid velocity) mountain. We then input the result into PLUTO as the starting point for time-dependent simulations which include thermal conduction. In the first stage we do not model growth of the mountain but rather solve for a self-consistent equilibrium (i.e. hydromagnetic force balance) given a certain amount of accreted mass and an EOS. Time-dependent simulations in the literature confirm that the equilibrium agrees closely with mountains built from scratch by injecting mass from below (Vigelius & Melatos 2009c; Wette et al. 2010).

We assume that the magnetic field \boldsymbol{B} may be described through an axisymmetric Chandrasekhar decompo-

sition without a toroidal component 1 for simplicity, i.e. \boldsymbol{B} takes the form

$$\boldsymbol{B} = \frac{\boldsymbol{\nabla}\psi}{r\sin\theta} \times \hat{\boldsymbol{e}}_{\varphi} \tag{3}$$

in spherical coordinates (r, θ, φ) , where $\psi(r, \theta)$ is a scalar flux function (Chandrasekhar 1956). The mountain equilibrium is determined by the force balance (Grad-Shafranov) equation (Payne & Melatos 2004; Mukherjee & Bhattacharya 2012)

$$\nabla p + \rho \nabla \phi + \Delta^2 \psi \nabla \psi = 0, \tag{4}$$

where Δ^2 denotes the Grad-Shafranov operator,

$$\Delta^{2} = \frac{1}{4\pi r^{2} \sin^{2} \theta} \left[\frac{\partial^{2}}{\partial r^{2}} + \frac{\sin \theta}{r^{2}} \frac{\partial}{\partial \theta} \left(\frac{1}{\sin \theta} \frac{\partial}{\partial \theta} \right) \right], \quad (5)$$

p is the fluid pressure, ρ is the mass density, and ϕ is the gravitational potential. For now, we assume that the accreted matter obeys a barotropic EOS, $p=p(\rho)$, once equilibrium is reached. Although neutron stars are expected to be non-barotropic (Goldreich & Reisenegger 1992), the barotropic and non-barotropic solutions to the Grad-Shafranov problem are broadly similar, even in magnetars (Mastrano et al. 2011, 2015).

For $p = p(\rho)$, equation (4) implies that ρ and ψ satisfy

$$0 = \frac{dp}{d\rho} \left(\frac{\partial \rho}{\partial r} \frac{\partial \psi}{\partial \theta} - \frac{\partial \rho}{\partial \theta} \frac{\partial \psi}{\partial r} \right) + \rho \left(\frac{\partial \phi}{\partial r} \frac{\partial \psi}{\partial \theta} - \frac{\partial \phi}{\partial \theta} \frac{\partial \psi}{\partial r} \right). \quad (6)$$

Equation (6) can be solved exactly using the Lagrange-Charpit method to yield (Courant & Hilbert 1953)

$$\int \frac{dp}{d\rho} \frac{d\rho}{\rho} = F(\psi) - (\phi - \phi_0), \qquad (7)$$

where ϕ_0 denotes a reference gravitational potential at the neutron star surface, and F is an arbitrary function of the scalar flux. Given $p = p(\rho)$, the integral in (7) can be evaluated, in principle, to express ρ in terms of ψ or vice-versa.

In order to obtain a one-to-one correspondence between the pre- and post-accretion states that respects flux-freezing, we demand that the steady-state, mass-flux ratio $dM/d\psi$, defined as the mass enclosed between the infinitesimally separated flux surfaces ψ and $\psi + d\psi$, equals that of the initial state plus any accreted matter (Alfvén 1943; Mouschovias 1974; Melatos & Phinney 2001). This restriction on $M(\psi)$ leads to the constraint (Payne & Melatos 2004)

$$\frac{dM}{d\psi} = 2\pi \int_{C} ds \rho \left[r(s), \theta(s) \right] r \sin \theta |\nabla \psi|^{-1}, \tag{8}$$

where C is the curve $\psi[r(s), \theta(s)] = \psi$ parametrized by the arc length s. Equation (8) can be solved by inverting (7) for ρ in terms of ψ given $p = p(\rho)$, leading to a unique expression for the function $F(\psi)$ given $M(\psi)$. The explicit forms of F

¹ Three-dimensional mountain equilibria for $M_a \gtrsim M_c$ are susceptible to Parker-like (Vigelius & Melatos 2008) and ballooning (Mukherjee et al. 2013b) instabilities with EOS-dependent growth rates (Kosiński & Hanasz 2006). However, the instabilities do not disrupt the mountain; they reduce the ellipticity by $\lesssim 30$ percent when they saturate (Vigelius & Melatos 2008). Furthermore, previous three-dimensional, time-dependent simulations reveal that the magnetic field relaxes to an almost axisymmetric configuration within a few Alfvén times (Payne & Melatos 2007; Vigelius & Melatos 2008).

for adiabatic and isothermal EOS can be found in Priymak et al. (2011) and Payne & Melatos (2004) respectively.

We solve (4) simultaneously with (8) numerically using the relaxation algorithm described in Payne & Melatos (2004) and later extended by Priymak et al. (2011). Specifically, the solver employs iterative under-relaxation combined with a finite-difference Poisson solver to solve (4) for ψ , obtain ρ from (8), and feed the result back into (4) iteratively, until convergence is achieved. Additional information regarding units, convergence, and stability can be found in the aforementioned papers and is not repeated here; see also Payne & Melatos (2007) and Vigelius & Melatos (2008). In accord with previous work, we prescribe the mass-flux distribution in one hemisphere to be (Melatos & Payne 2005)

$$M(\psi) = \frac{M_a \left[1 - \exp(-\psi/\psi_a)\right]}{2 \left[1 - \exp(-b)\right]},\tag{9}$$

where M_a is the accreted mass, ψ_a labels the field line at the polar-cap boundary (that closes just inside the inner edge of the accretion disc), and we define $b = \psi_{\star}/\psi_a$, where ψ_{\star} labels the total hemispheric flux. Throughout this paper we set b=3 to ensure numerical stability.

For simplicity we assume a constant gravitational acceleration, with $\phi(r) = GM_{\star}r/R_{\star}^2$, where R_{\star} is the stellar radius, and make the Cowling approximation (i.e. we ignore self-gravity). These assumptions are justified, because the mountain never rises more than $\sim 10^4$ cm above the surface at $r = R_{\star}$, and we consider systems with $M_a/M_{\odot} \lesssim 10^{-1}$ [see section 2.1 of Priymak et al. (2011)]. Additionally, Haskell et al. (2006) and Yoshida (2013) found that the Cowling approximation alters the mass ellipticity by at most a factor of ~ 3 even for the strongest magnetar fields ($\lesssim 10^{16}$ G).

Equation (4) is solved subject to physically motivated boundary conditions, which carry through to the evolution experiments in PLUTO in Sec. 2.4 (see also Appendix A). Following previous work, we set $\psi(R_{\rm in}, \theta) = \psi_{\star} \sin^2 \theta$ (surface dipole), $\partial \psi / \partial r(R_{\rm m}, \theta) = 0$ (Neumann outflow²), $\psi(r, 0) = 0$ (straight polar field line), and $\partial \psi / \partial \theta(r, \pi/2) = 0$ (equatorial symmetry), where $R_{\rm in} \leqslant r \leqslant R_{\rm m}$ and $0 \leqslant \theta \leqslant \pi/2$ demarcate the computational volume (Payne & Melatos 2004; Melatos & Payne 2005; Vigelius & Melatos 2008; Priymak et al. 2011). The outer radius $R_{\rm m}$ is chosen large enough

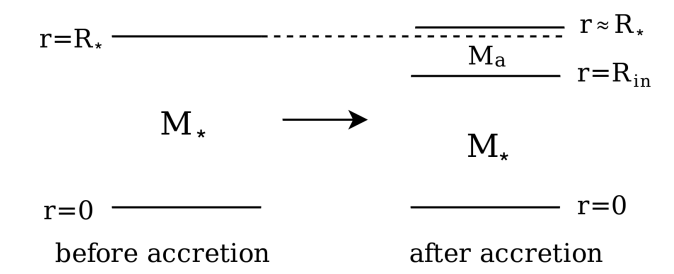


Figure 2. Schematic diagram (not to scale) of the radial computational setup, described in Sec. 2.2, of an accreted crust on a neutron star. The inner computational boundary $R_{\rm in}$ is determined by $M_a = \int_{r=R_{\rm in}}^{r=R_{\star}} d^3x \, \rho$. If sinking is included in the model (see Sec. 2.3), the mountain height reduces on the hydrostatic settling time-scale.

to encompass all the screening currents and the outer edge of the accreted matter; we set $R_{\rm m}=1.4R_{\star}$ throughout this paper. The boundary conditions on ψ are reformulated as conditions on \boldsymbol{B} through (3) and conditions on ρ (and hence p) through (8). In the time-dependent PLUTO simulations (see Sec. 2.4) we also stipulate no slip at $R_{\rm in}$, outflow at $R_{\rm m}$, and reflecting boundary conditions on \boldsymbol{v} at the equator.

Although $R_{\rm in}$ is treated as a hard surface for simplicity, it is not so in reality; a mountain several tens of meters high, whose base reaches neutron drip densities, sinks into the lower-density substrate (Wette et al. 2010; Priymak et al. 2011). A full treatment of sinking requires time-dependent simulations. Wette et al. (2010) showed that the results are approximated reasonably by hard-surface solutions (the mountain ellipticity decreases by a factor $\lesssim 2$ for soft crust solutions relative to hard-surface solutions), if $R_{\rm in}$ corresponds to the layer above which the mass equals M_a ; i.e. one has $R_{\rm in} < R_{\star}$ and $M_a = \int_{r=R_{\rm in}}^{r=R_{\star}} d^3 \boldsymbol{x} \, \rho$. As $R_{\rm in}$ is fixed, the stellar radius R_{\star} varies slightly ($\leqslant 1$ per cent for $M_a \leqslant 10^{-4} M_{\odot}$) between models with different M_a but the same EOS. Figure 2 visually demonstrates the relationship between $R_{\rm in}$, R_{\star} , and M_a .

2.3 Equation of state

Crustal matter experiencing compression due to accretion undergoes a variety of non-equilibrium nuclear processes, such as electron captures and beta decay, neutron emission and absorption, and pyconuclear fusion, all of which play a role in determining the EOS of the accreted crust (Sato 1979; Miralda-Escude et al. 1990; Chamel & Haensel 2008). The original outer crust, consisting of cold, catalysed matter, is replaced by a new, non-catalysed crust after $\leq 10^{5}$ yr (Haensel & Zdunik 1990a). The EOS of an accreted, noncatalysed crust, relevant for our calculations, has been calculated numerically by Haensel & Zdunik (1990b) by modeling the non-equilibrium processes listed above, using the compressible liquid drop model of Mackie & Baym (1977) to estimate the various thermodynamic rates which feed into the Gibbs equation [see also Sec. 2.4 of this paper and Bisnovatyi-Kogan & Chechetkin (1979)].

In this paper we consider three idealized yet physically motivated polytropic EOS: a single-index model which best approximates (in a least-squares sense; see below) a realistic accreted crust (model A), and two of the classical ideal gas

² Ideally, this condition would be replaced by a dipolar field condition at the outer edge, i.e. $\psi(R_{\rm m},\theta) = \psi_{\rm m} \sin^2 \theta$ for some value of $\psi_{\rm m}$, so as not to introduce artificial magnetic multipoles (including a monopole) far from the stellar surface. However, in order to assign a value to $\psi_{\rm m}$, as necessary for numerical computation, we need to know by how much magnetic burial reduces the dipole moment, with $\mu/\mu_i \propto \psi_{\rm m}/\psi_i$. In principle, it is possible to adjust $\psi_{\rm m}$ iteratively in order to obtain a self-consistent simulation, but this is technically challenging (see also Footnote 4). A thorough discussion of the issue can be found in Sec. 4.3 of Vigelius & Melatos (2008) and in Sec. 4.1 of Payne & Melatos (2007), as well as references therein. In particular, Vigelius & Melatos (2008) showed that the density distribution (Fig. 14 of the latter reference, left panel) is virtually indistinguishable between Neumann and dipole condition equilibria, while the magnetic field lines (right panel) tend to agree except in the outermost regions, where the plasma density is low. The Neumann outflow condition artificially increases μ , relative to corresponding ZEUS equilibria, by $\lesssim 10\%$ [see Fig. 3(f) of Payne & Melatos (2007)].

models considered by Priymak et al. (2011), corresponding to a gas of non-relativistic degenerate electrons (model B), and a gas of non-relativistic degenerate neutrons (model C). Their parameters are summarised in Table 1; see also Privmak et al. (2011). Models A, B, and C apply only at t=0; they are used to construct initial conditions for PLUTO. The Grad-Shafranov solver developed by Priymak et al. (2011) quasi-statically determines the 'end-state' of an adiabatic accretion process in the absence of thermal conduction. As noted above, we initialise PLUTO with an M_a -dependent Grad-Shafranov equilibrium to avoid numerical difficulties, cf. Wette et al. (2010). In reality, however, the true endstate of accretion depends on \dot{M}_a as well as M_a . Accreted plasma on the stellar surface is expected to be approximately isothermal ($\Gamma \approx 1$) at all depths for low-accretion rates $\dot{M}_a \lesssim 10^{-10} \dot{M}_{\odot} \text{ yr}^{-1}$ (Fujimoto et al. 1984; Zdunik et al. 1992). In contrast, a crust formed on a star accreting near the Eddington limit $\dot{M}_a \gtrsim 10^{-8} M_{\odot} \text{ yr}^{-1}$ has a more complicated polytropic EOS with a depth-dependent adiabatic index $(1 \lesssim \Gamma \lesssim 5/3)$ (Brown & Bildsten 1998; Brown 2000). Hence the time-dependent accretion process, which is not modeled here except implicitly through (9), directly affects the softness or hardness of the EOS. In particular, a self-consistent model of accretion along the lines of the sinking problem treated by Wette et al. (2010) would lead to end-state values of k_{Γ} and Γ which depend on both M_a and \dot{M}_a (Fujimoto et al. 1984; Brown et al. 1998). The numerical experiments we conduct in PLUTO, which evolve the EOS via thermal conduction, partially account for the effects of a near-Eddington accretion rate on the crustal EOS a posteriori (see Sec. 2.4). This procedure has been validated in the absence of thermal conduction by Wette et al. (2010).

In Figure 3 we graph pressure-density relationships for models A, B, and C (broken curves) together with the numerical results of Haensel & Zdunik (1990b) (solid curve). For $\rho\gtrsim1.5\times10^{13}~{\rm g~cm^{-3}},$ the maximum density computed by Haensel & Zdunik (1990b), we graph the innercrust model of Douchin & Haensel (2001), also computed using the compressible liquid drop model (Mackie & Baym 1977). Denoting the neutron drip density by $\rho_{\rm nd}$ [$\rho_{\rm nd}$ ~ 5×10^{11} g cm⁻³ in an accreted crust (Chamel et al. 2015)], we see that the numerical results are approximated adequately by models B and C used in previous work (Priymak et al. 2011) in the regimes $\rho \ll \rho_{\rm nd}$ and $\rho \gtrsim \rho_{\rm nd}$ respectively. On the other hand, model A is constructed to uniformly approximate the realistic EOS for all $\rho \lesssim 10^{14} \ \mathrm{g \ cm^{-3}}$. The parameters k_{Γ} and Γ for model A are computed by fitting $p(\rho) = k_{\Gamma} \rho^{\Gamma}$ with the Levenberg-Marquardt (damped least-squares) algorithm (Press et al. 1986) to the data collated in Table 1 of Haensel & Zdunik (1990b). Denoting the Haensel & Zdunik (1990b) numerical pressure by $p^{\rm HZ}$ and the model A pressure by p^{A} , the fit yields relative errors of $0.94 \leqslant p^{\rm HZ}/p^{\rm A} \leqslant 2.51$ for $10^8 \leqslant \rho/{\rm g~cm^{-3}} \leqslant 10^{14}$. Throughout most of the mountain volume by mass, i.e. for $\rho \geqslant 10^{12} \ \mathrm{g \ cm^{-3}}$, the errors drop to $\leqslant 6$ percent, with $0.95 \leqslant p^{\mathrm{HZ}}/p^{\mathrm{A}} \leqslant 1.06$. For $\rho \leqslant 10^9 \ \mathrm{g \ cm^{-3}}$ we have $0.94 \leqslant p^{\mathrm{HZ}}/p^{\mathrm{A}} \leqslant 1.07$.

A piecewise polytropic fit to the solid curve in Fig. 3 (e.g. a spline fit to $\log p$ vs $\log \rho$) is a better approximation than the uniform, $\Gamma = 1.18$ fit in model A. As a practical matter, however, it is difficult to generalise the Grad-Shafranov calculation in Sec. 2.2, especially the explicit for-

Table 1. EOS parameters for numerical mountain models. We assume a polytropic, single-index EOS with $p(\rho)=k_{\Gamma}\rho^{\Gamma}$, where k_{Γ} is measured in cgs units (dyn g^{-\Gamma} cm^{3\Gamma-2}) (Shapiro & Teukolsky 1983; Priymak et al. 2011).

Model	k_{Γ} (cgs)	Γ	EOS
A B C	6.18×10^{15} 3.16×10^{12} 5.38×10^{9}	1.18 5/3 5/3	Realistic accreted crust Isentropic gas; degenerate e^- Isentropic gas; degenerate n

mula for $F(\psi)$ [equation (8) in Priymak et al. (2011)], to apply to multiple layers with proper matching at the inter-layer boundaries. As the Grad-Shafranov calculation is an essential input to the PLUTO simulations, the uniform $\Gamma=1.18$ approximation is the best we can do for now. For this reason, among others, the final results should be viewed as qualitatively representative models of the thermal conduction physics rather than quantitatively accurate mountain models to be compared in detail to observational data.

Different EOS predict different maximum (base) densities ρ_{max} and heights H for any given M_a . In Table 2 we list the characteristic ρ_{max} and H for runs performed in this paper (see Sec. 3.2) together with a rough estimate for the expected depth within a neutron star to which $\rho_{\rm max}$ corresponds. Note that the sinking depths listed in Table 2 apply for stellar mass $M_{\star} = 1.4 M_{\odot}$, and a Skyrme-type EOS at zero temperature, used to describe both the crust and the liquid core, based on the effective nuclear interaction SLy (Douchin & Haensel 2001). Different EOS and stellar masses lead to different sinking depths. For models A and C, the theoretical depth exceeds the simulated height of the mountain. Depending on the crustal elasticity (Chamel & Haensel 2008), this indicates that mountain matter should sink beneath the surface and influence the hydromagnetic structure of the star (Konar & Choudhuri 2002). However, using breaking strain arguments, it has been shown that realistic crustal ellipticites of neutron stars cannot exceed $\sim 10^{-6}$ (Haskell et al. 2006; Johnson-McDaniel & Owen 2013), which is less than those associated with accreted mountains (see Sec. 4.2). As such, any gravitational radiation due to crustal quadrupole moment generation via back-reaction effects from a sinking mountain is likely to be dwarfed by the radiation due to the mountain itself (Wette et al. 2010), though there may be interesting consequences for other phenomena, e.g. crust-core coupling (Glampedakis & Andersson 2006). The lateral (θ) structure of the mountain is not affected greatly by sinking, as shown by Wette et al. (2010). Hence the main effect of sinking on ϵ is to reduce it by a factor $\approx (R_{\rm pre}/R_{\rm post})^5$, where $R_{\rm pre}$ and $R_{\rm post}$ are the characteristic radii of the base of the mountain before and after sinking, respectively, and "before sinking" here means "in the context of a hard-surface Grad-Shafranov calculation". In any case, because we do not model sinking, the values of the ellipticities (and heights) presented in this paper should be taken as upper limits. Modeling a realistic neutron star together with a sinking mountain in a way that simultaneously tracks the Alfvén and sinking time-scales is a difficult problem that will be considered in future work.



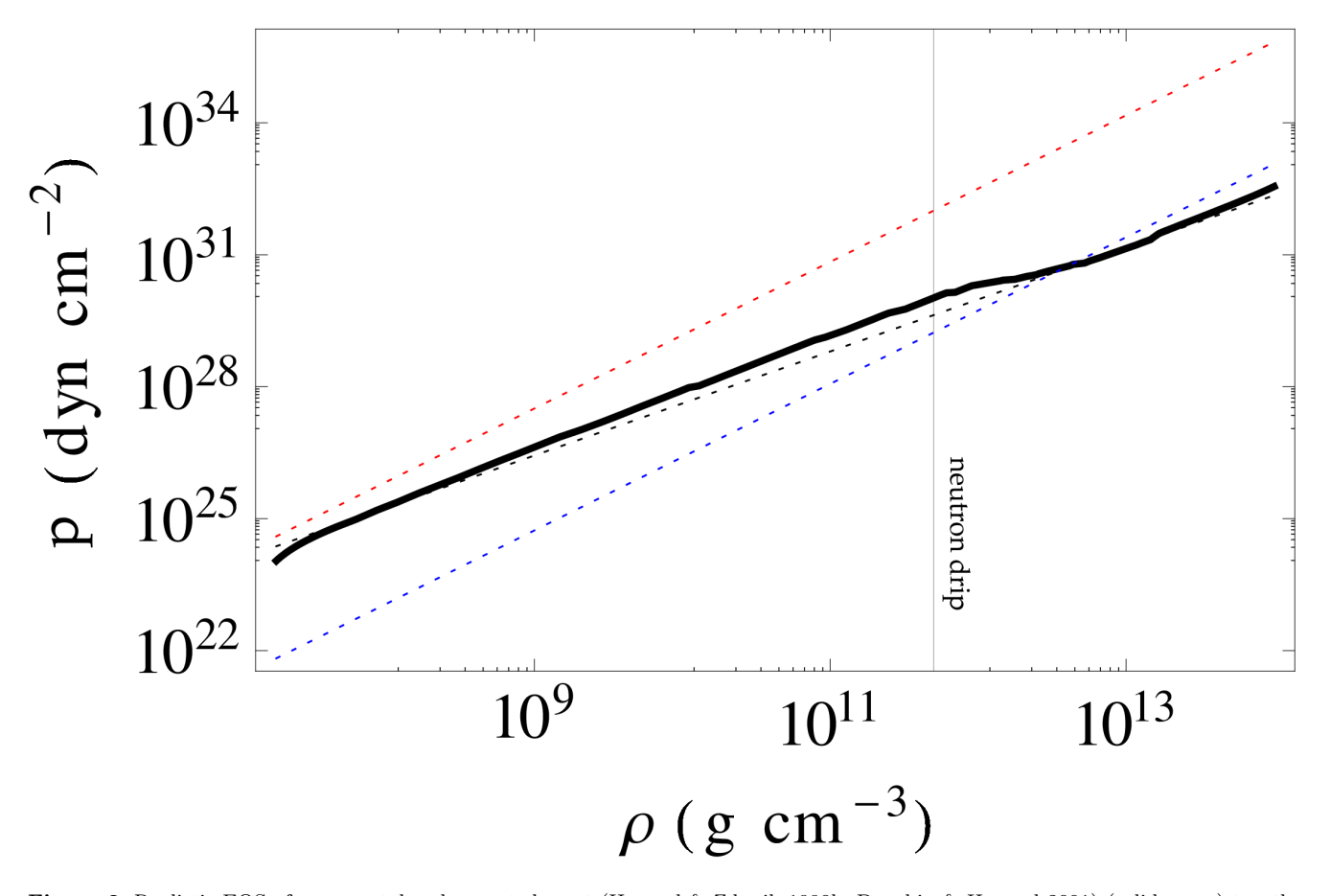


Figure 3. Realistic EOS of a non-catalysed, accreted crust (Haensel & Zdunik 1990b; Douchin & Haensel 2001) (solid curve) together with the approximate, single-index EOS used in this paper: model A (black dashed curve), model B (red dashed curve), and model C (blue dashed curve). For reference, the neutron drip density [$\sim 5 \times 10^{11}$ g cm⁻³ in an accreted crust (Chamel et al. 2015)] is shown by a vertical line.

Table 2. Characteristic maximum density, mountain height, and approximate depth beneath the surface where the pre-accretion density is $\rho_{\rm max}$ (i.e. characteristic sinking depth), estimated for a neutron star of mass $M_{\star}=1.4M_{\odot}$ with a Skyrme EOS.

Model	$\rho_{\rm max}({\rm g~cm^{-3}})$	Height (cm)	Sinking depth (cm)
A B	2×10^{13} 8×10^{8}	3×10^3 4×10^4	$\sim 10^4 - 10^5$ $\sim 10^3 - 10^4$
$^{\mathrm{C}}$	3×10^{11}	5×10^3	$\sim 10^4 - 10^5$

2.4 MHD evolution

The steady-state solution to the Grad-Shafranov problem in section 2.2 serves as initial data for evolving the mountain dynamically. In the absence of viscosity and under the assumptions of infinite electric conductivity³ (ideal MHD)

 3 The Ohmic diffusion and thermal conduction time-scales (see Sec. 2.5) are in the ratio $\tau_{\rm d}/\tau_{\rm c}\approx 2\times 10^{-14}\left(\sigma/\ {\rm s}^{-1}\right)|B|/|\nabla^2 B|L^{-2}\left(\rho/10^{10}\ {\rm g\ cm}^{-3}\right)^{-1},$ for characteristic length-scale L and electrical conductivity $\sigma.$ In the crust-magnetosphere interface, one has $\sigma\lesssim 10^{16}\ {\rm s}^{-1}$ (Akgün et al. 2018). In the inner crust one has $\sigma\gtrsim 10^{24}\ {\rm s}^{-1}$ (Potekhin 1999; Potekhin et al. 2013). Hence we find $\tau_{\rm d}/\tau_{\rm c}\gg 1$ throughout the computational volume for the range of accreted masses

and the Cowling approximation, the evolution is governed by the continuity, Euler, and Faraday equations, which read (Landau & Lifshitz 1959)

$$0 = \frac{\partial \rho}{\partial t} + \boldsymbol{\nabla} \cdot (\rho \boldsymbol{v}), \qquad (10)$$

$$0 = \rho \frac{\partial \mathbf{v}}{\partial t} + \rho \left(\mathbf{v} \cdot \mathbf{\nabla} \right) \mathbf{v} + \mathbf{\nabla} p + \rho \mathbf{\nabla} \phi$$
$$- \left(4\pi \right)^{-1} \left[\left(\mathbf{\nabla} \times \mathbf{B} \right) \times \mathbf{B} \right], \tag{11}$$

and

$$0 = \frac{\partial \boldsymbol{B}}{\partial t} - \boldsymbol{\nabla} \times (\boldsymbol{v} \times \boldsymbol{B}), \qquad (12)$$

considered in this paper, even in regions with strong magnetic gradients, because the density is low there ($\rho \lesssim 10^{10} \ {\rm g \ cm^{-3}}$). We can therefore safely ignore the effects of Ohmic diffusion over the time-scales simulated within this paper; see also Vigelius & Melatos (2009c).

respectively, given ϕ . The MHD equations (10)–(12) are closed by the energy equation,

$$\nabla \cdot \mathbf{F} = \nabla \cdot \left[\left(\varepsilon + \frac{\rho \mathbf{v}^2}{2} + p + \frac{\mathbf{B}^2}{4\pi} + \rho \phi \right) \mathbf{v} - \frac{\mathbf{B} \left(\mathbf{v} \cdot \mathbf{B} \right)}{4\pi} \right] + \frac{\partial}{\partial t} \left(\varepsilon + \frac{\rho \mathbf{v}^2}{2} + \frac{\mathbf{B}^2}{8\pi} + \rho \phi \right), \tag{13}$$

where T is the temperature, \boldsymbol{F} is the heat flux, and ε is the internal energy (Shapiro & Teukolsky 1983). The kinetic properties of the fluid determine the internal energy in terms of the thermodynamic variables p, ρ , and temperature T, i.e. $\varepsilon = \varepsilon(p, \rho, T)$ (Kundu & Cohen 2008). The Gibbs fundamental equation,

$$0 = TdS - pdV - d\varepsilon \tag{14}$$

$$= TdS - pdV - \left(\frac{\partial \varepsilon}{\partial p} dp + \frac{\partial \varepsilon}{\partial \rho} d\rho + \frac{\partial \varepsilon}{\partial T} dT\right), \qquad (15)$$

where V is the system volume and S is the entropy, provides an additional constraint for the state variables. We then have seven scalar equations, namely (10)–(14), for seven variables in the axisymmetric problem: $p, \rho, T, B_r, B_\theta, v_r$, and v_θ . In practice, (15) determines T given p and ρ , while (13) determines the the relationship between p and ρ , i.e. the barotropic EOS $p = p(\rho)$ initially. Under the assumption of an ideal gas (consistent with a polytropic EOS), equation (15) leads to the well-known relation (Shapiro & Teukolsky 1983)

$$T = \frac{\eta m_u p}{k_B \rho},\tag{16}$$

where η is the mean molecular weight, m_u is the atomic mass unit and k_B is the Boltzmann constant. The temperature field $T(p,\rho)$ in (16) is calculated from the Grad-Shafranov output and forms an additional input into PLUTO for thermal conduction simulations. We make the assumption of symmetric nuclear matter to determine η for simplicity as in previous work [see section 2.3 of Priymak et al. (2011)]. Although the ideal gas law (16) is modified in degenerate matter, it provides a good approximation for partially-degenerate, accreted material on a neutron star crust (Schatz et al. 1999) and is straightforward to handle within PLUTO. A sensitivity analysis associated with expression (16) is presented in Appendix B, where it is shown that using (16) to determine T as opposed to a degenerate EOS calculated from first principles overestimates the temperature by $\lesssim 15\%$ throughout the bulk of the mountain (see also Secs. 2.3 and 3), where thermal transport matters most; a small effect compared to other uncertainties in the problem.

2.5 Thermal conduction

In the presence of thermal conduction, the flux on the left-hand side of (13) takes the form (Landau & Lifshitz 1959)

$$\mathbf{F} = \kappa_{||} \hat{\mathbf{B}} (\hat{\mathbf{B}} \cdot \nabla T) + \kappa_{\perp} [\nabla T - \hat{\mathbf{B}} (\hat{\mathbf{B}} \cdot \nabla T)], \tag{17}$$

where the thermal conductivities $\kappa_{||}$ and κ_{\perp} , both measured in units of erg s⁻¹ K⁻¹ cm⁻¹, describe heat transport parallel and perpendicular to the magnetic field respectively. The conductivities of a magnetised, fully ionized plasma are dominated by electron transport. They are given in the diffusion approximation by the Balescu-Braginskii formulas [see

Braginskii (1965); Potekhin (1999) and Table 3.2 of Balescu (1988)],

$$\kappa_{||} \approx 1.77 \times 10^{16} \left(\frac{T_e}{10^9 \text{ K}} \right)^{5/2} \text{erg s}^{-1} \text{ K}^{-1} \text{ cm}^{-1}, \quad (18)$$

and

$$\kappa_{\perp} \approx \kappa_{||} \left[1 + 1.19 \left(\frac{\rho}{10^{10} \text{ g cm}^{-3}} \right)^{-2} \left(\frac{|\mathbf{B}|}{5 \times 10^{13} \text{ G}} \right)^{2} \right] \times \left(\frac{T_{e}}{10^{9} \text{ K}} \right)^{3} \right]^{-1} \text{erg s}^{-1} \text{ K}^{-1} \text{ cm}^{-1},$$
 (19)

assuming the Coulomb logarithm satisfies $\ln \Lambda = 30 \approx \text{constant}$ (Balbus 1986). The estimates (18) and (19) are independent of the ideal gas assumption (16). In the limit of a vanishing magnetic field, one has $\kappa_{\perp} = \kappa_{||}$, and (17) reduces to $F = \kappa_{||} \nabla T$.

2.6 Time-scales

A mountain with the structure in Fig. 1 contains steep density and magnetic field gradients, so there is no unique definition for characteristic time-scales, like the Alfvén time $\tau_{\rm A}$ and thermal conduction time $\tau_{\rm c}$. In order to analyse our numerical results in Sec. 3 onwards, we adopt the definition (Mukherjee & Bhattacharya 2012)

$$\tau_{\rm A} = L\sqrt{4\pi\bar{\rho}}/|\bar{B}| \qquad (20)$$

$$\approx 7 \times 10^{-5} \left(\frac{L}{10^4 \text{ cm}}\right) \left(\frac{\bar{\rho}}{10^{10} \text{ g cm}^{-3}}\right)^{1/2}$$

$$\times \left(\frac{|\bar{B}|}{5 \times 10^{13} \text{ G}}\right)^{-1} \text{ s}, \qquad (21)$$

where L is taken to be the density scale-height where ρ drops to 10^{-3} times its maximum value $\rho_{\rm max}$, $\bar{\rho}$ is the volume-averaged density

$$\bar{\rho} = \frac{1}{V_{\rm m}} \int d^3 \boldsymbol{x} \, \rho, \tag{22}$$

where $V_{\rm m}$ is the mountain volume $(10^{-7}\rho_{\rm max} \leqslant \rho \leqslant \rho_{\rm max})$ and $|\bar{\boldsymbol{B}}|$ is the volume-averaged magnetic field strength,

$$|\bar{\boldsymbol{B}}| = \frac{1}{V_{\rm m}} \int d^3 \boldsymbol{x} \, |\boldsymbol{B}|. \tag{23}$$

All the quantities (20)–(23) are computed at t=0 to define $\tau_{\rm A}$ for any given run. Similarly, for thermal conduction, from the heat equation we have

$$\tau_{\rm c} = \frac{5}{3} (L/1 \text{cm})^2 (\bar{\rho}/\text{ g cm}^{-3})$$

$$\times [\bar{\kappa}_{||}/\text{erg s}^{-1} \text{ K}^{-1} \text{ cm}^{-1}]^{-1} \text{ s} \qquad (24)$$

$$\approx 94.2 \left(\frac{L}{10^4 \text{ cm}}\right)^2 \left(\frac{\bar{\rho}}{10^{10} \text{ g cm}^{-3}}\right) \left(\frac{\bar{T}_e}{10^9 \text{ K}}\right)^{-5/2} \text{ s}, \qquad (25)$$

where $\bar{\kappa}_{\perp}$, $\bar{\kappa}_{||}$, and \bar{T}_e are volume-averaged quantities calculated in the same manner as $\bar{\rho}$ in (22) and $|\bar{B}|$ in (23).

The thermal conduction time is $\sim 10^6$ times longer than the Alfvén time for a typical, realistic mountain. Computational expense restricts us to $t \lesssim 2\tau_c$ throughout most of this paper (see Sec. 3). The ratio of the time-scales varies from

run to run and for different EOS. We perform some 'long-term' evolutions (up to $\sim 80\tau_{\rm c}$) in Section 5 to explore the effects of thermal relaxation. In Sections 3 and 4 we show that (21) and (25) agree with the time-scales of characteristic behaviours observed empirically in the simulations.

3 THERMAL EVOLUTION

PLUTO (Mignone et al. 2007) is a general-purpose MHD solver designed to handle steep gradients associated with strong shock phenomena in astrophysical applications. It solves (10)–(13) given the Grad-Shafranov solution and the boundary conditions described in Sec. 2.2 as inputs. The details of the computation are presented in Appendix A along with convergence tests.

In this section we present results from PLUTO simulations of magnetic mountain evolution on time-scales comparable to τ_c . We load a Grad-Shafranov equilibrium calculated in Sec. 2.2 for some equation of state (e.g. A,B, or C in Table 1) into PLUTO and evolve it in two ways, with thermal conduction switched on or off, to explore the mass density and magnetic field profiles for a variety of runs (Sec. 3.2), the evolution of the thermal flux (Sec. 3.3), and the evolution of global observables like μ (Sec. 4.1) and ϵ (Sec. 4.2).

Several numerical and physical issues affect the PLUTO output. (i) The Grad-Shafranov code computes ψ , while PLUTO accepts the components of \boldsymbol{B} . The calculation of \boldsymbol{B} from ψ involves differentiation, which introduces some numerical error. We use PLUTO's inbuilt bi-linear interpolation algorithm to map the Grad-Shafranov output to PLUTO input (see Appendix A). (ii) PLUTO maintains ideal-MHD flux freezing through a Godunov scheme [e.g. Gardiner & Stone (2005)], but it does not act directly to satisfy the integral constraint (8) on $M(\psi)$. As $M(\psi)$ is not an input into PLUTO, and equation (8) is a non-linear equation for ψ , it is possible that multiple, valid solutions for ψ exist at any given t. One can imagine PLUTO picking a solution branch unpredictably based on numerical fluctuations, if two valid solutions for ψ are numerically close. (iii) The Grad-Shafranov equilibrium may not represent the stable endpoint of a well-posed initial value problem because the Grad-Shafranov equation has multiple unstable solutions (Payne & Melatos 2007). This is related to the loss-of-equilibrium phenomenon investigated by Klimchuk & Sturrock (1989).

3.1 Representative example

We start by considering a representative simulation, which demonstrates the main features of thermal evolution: EOS model A with $M_a = 1.8 \times 10^{-5} M_{\odot} \approx 0.58 M_c$. We set up a polytropic initial state ($\Gamma = 1.18$ at t = 0), allow thermal conduction to take place, and evolve the mountain. The EOS parameters, described in Table 1, are entered into the Grad-Shafranov solver, which produces the initial input for PLUTO. The thermal profile is entered according to (16). Two separate PLUTO instances are evolved, with and without the thermal flux \boldsymbol{F} appearing in the right-hand side of equation (13). The time-scales (21) and (25) read $\tau_{\rm A} \approx 2.0 \times 10^{-5}$ s and $\tau_{\rm c} \approx 5.6 \times 10^6 \tau_{\rm A}$.

In Figure 4, which demonstrates several features typical of an initially polytropic mountain, we graph contours of ρ and magnetic field lines at t=0. The mountain reaches a maximum altitude of $H_{\rm max}\approx 1.3\times 10^3$ cm near $\theta=\pi/4$ (where $|{\bf B}|$ rises to a maximum). Most of the mass ($\approx 92\%$) is concentrated within the octant $0 \le \theta \le \pi/4$. The densest point, with $\rho=2.2\times 10^{13}$ g cm⁻³, lies at the pole. The magnetic field lines are shifted equatorially; the maximum contour lies at $\theta=\pi/4$, in contrast to the initial dipole field (maximum at $\theta=0$).

Figure 5 presents results from PLUTO and illustrates how thermal conduction affects the evolution. It shows snapshots at $t = 2\tau_c$ of an adiabatic mountain ($\mathbf{F} = 0$, left panel) and one evolved with a nonzero thermal flux ($\mathbf{F} \neq 0$, right panel). The mountain grows from $H_{\rm max} \approx 1.3 \times 10^3 {\rm cm}$ to $H_{\rm max} \approx 3.0 \times 10^3$ cm. It is $\approx 4\%$ taller for the run with conduction, but its density is lower (by a factor ≤ 5 near $\theta = 0.1$ where an underdense column forms; see Sec. 3.2) everywhere except at $\theta \approx 0$ and $\theta \approx 0.2$. This is a consequence of the continuity equation (10), which demands that an increase in height is met with an overall decrease in mass density. Aside from the underdense column, thermal conduction has the effect of driving matter towards the pole, where the density attains a maximum of $\rho_{\rm max}=1.3\times 10^{13}~{\rm g~cm^{-3}}$ for the run without conduction (left panel) and $\rho_{\rm max} = 1.5 \times 10^{13} \ {\rm g \ cm^{-3}}$ for the run with conduction (right panel) ($\approx 16\%$ increase). An analogous thermal softening phenomenon occurs in crustquake models, where thermal transport amplifies shear stresses felt in the neutron star crust (Chugunov & Horowitz 2010; Beloborodov & Levin 2014).

Evolution with $F \neq 0$ tends to widen the magnetic field contours (cf. Fig. 4), because the mountain spreads and drags the field-lines with it [the time-dependent version of the flux-freezing condition (8)]. Thermal conduction causes matter to be shifted both towards the pole and towards the base of the mountain, causing magnetic 'pockets' to form near $\theta=0$ (see also Sec. 3.2 and Fig. 6, where they are clearer), as the field lines bend around the drifting matter. Overall, the magnetic field is weakened, going from a maximum strength of $|{\bf B}|_{\rm max}=2.9\times10^{15}~{\rm G}$ to $|{\bf B}|_{\rm max}=1.9\times10^{15}~{\rm G}$ and $|{\bf B}|_{\rm max}=2.0\times10^{15}~{\rm G}$ at $t=2\tau_{\rm c}$ without and with conduction, respectively. Away from the pole, the locations of the maxima and minima of $|{\bf B}|$ are largely unaffected by conduction.

3.2 Mass density and magnetic field evolution

In Figure 6 we plot ρ contours and magnetic field lines for model A (top row) with $M_a=2.4\times 10^{-5}M_{\odot}\approx 1.0M_c$, model B (middle row) with $M_a=3.0\times 10^{-8}M_{\odot}\approx 1.2M_c$, and model C (bottom row) with $M_a=2.0\times 10^{-6}M_{\odot}\approx 1.0M_c$ for times t=0 (left panel) and $t=2\tau_c$ without (middle panel) and with (right panel) thermal conduction. The initial state is read from the Grad-Shafranov output and is the same for both runs for any given EOS. All three runs have similar⁴ values of $M_a/M_c\sim 1$, implying that μ

 $^{^4}$ Ideally we would keep M_a/M_c exactly the same across all runs. However, this is impractical because one does not know what μ

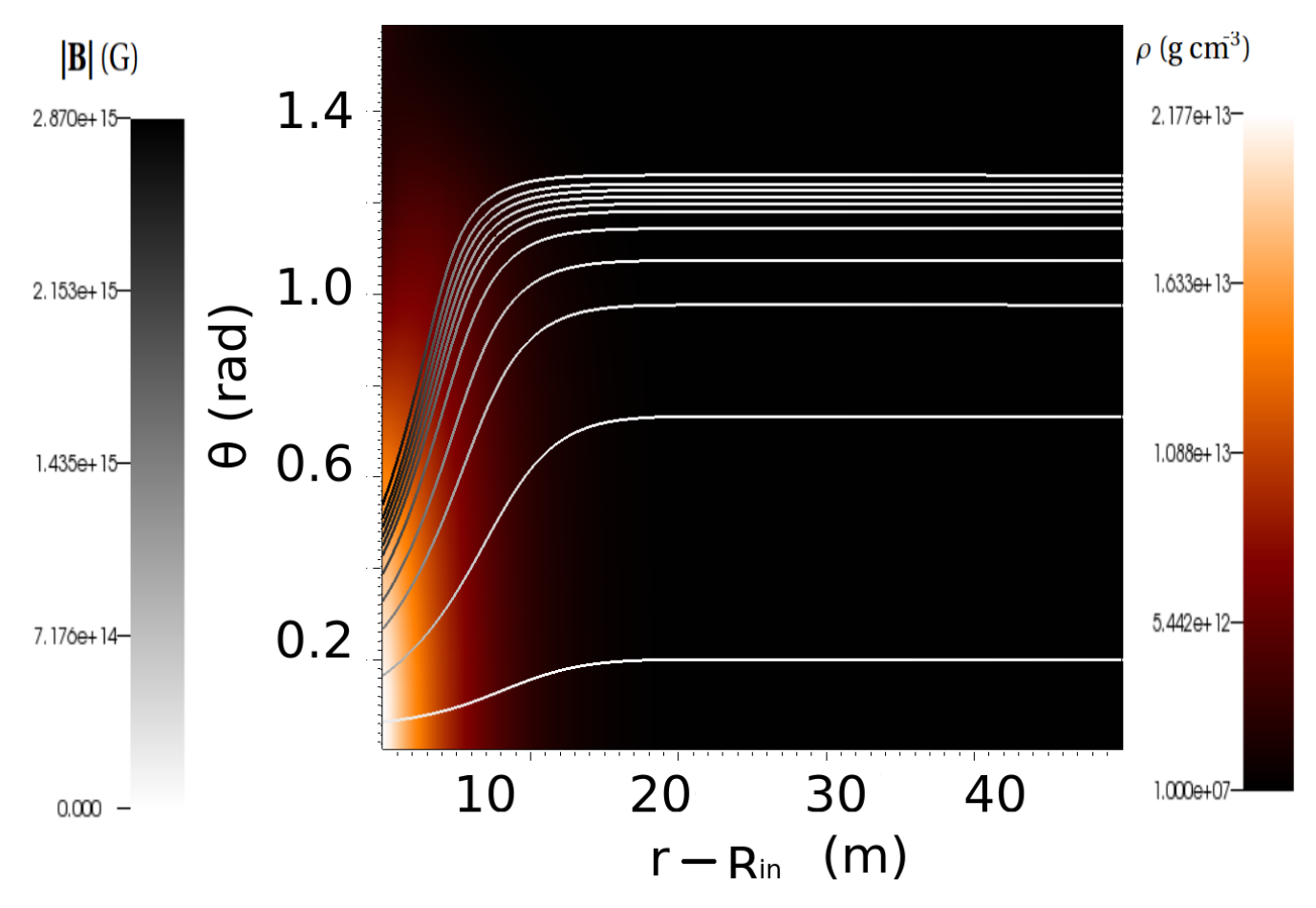


Figure 4. Density ρ (colour scale; brighter shades indicate higher ρ) and magnetic field lines (darker shades indicate higher $|\mathbf{B}|$) for the realistic accreted crust model A with accreted mass $M_a = 1.8 \times 10^{-5} M_{\odot} \approx 0.58 M_c$ at time t = 0, plotted as functions of altitude (horizontal axis) and colatitude (vertical axis).

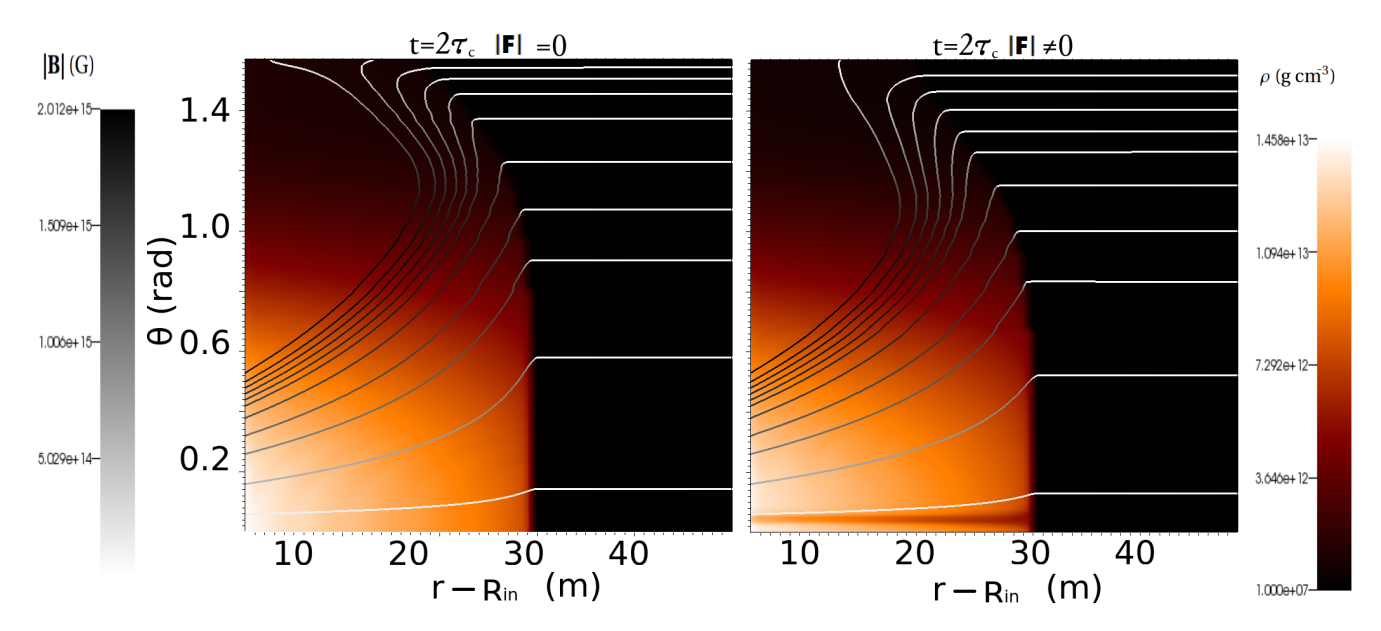


Figure 5. Density ρ (colour scale; brighter shades indicate higher ρ) and magnetic field lines (darker shades indicate higher $|\mathbf{B}|$) for the realistic accreted crust model A with accreted mass $M_a = 1.8 \times 10^{-5} M_{\odot} \approx 0.58 M_c$ with heat flux $\mathbf{F} = 0$ (left panel) and $\mathbf{F} \neq 0$ (right panel), plotted as functions of altitude (horizontal axis) and colatitude (vertical axis). The snapshots are taken at time $t = 2\tau_c$.

at t=0 is approximately halved by burial in all three models (see Sec. 4.1). We emphasise that models B and C are poor approximations to a realistic crust. They are included throughout mainly to give the reader a general sense of how the mountain structure depends on the EOS as well as to make contact with previous work for completeness.

The model A mountain (top row of Fig. 6) grows taller over time, thereby reducing $\bar{\rho}$; we find $H_{\rm max}=3.3\times 10^3$ cm for both F=0 and $F\neq 0$ at $t=2\tau_{\rm c}$, compared to $H_{\rm max}=1.2\times 10^3$ cm at t=0. The magnetic pole remains the densest region with maximum densities $\rho_{\rm max}=2.38\times 10^{13}$ g cm⁻³ at t=0 and $\rho_{\rm max}=1.43\times 10^{13}$ g cm⁻³ at $t=2\tau_{\rm c}$ without thermal conduction and $\rho_{\rm max}=1.45\times 10^{13}$ g cm⁻³ at $t=2\tau_{\rm c}$ with thermal conduction. A narrow, underdense ($\rho\lesssim 4\times 10^{12}$ g cm⁻³) column forms at $\theta\approx 0.1$ for the run with thermal conduction. Field lines are noticeably distorted from their t=0 state by flux freezing through a combination of poleward flow, which pushes them towards $\theta=0$, and stretching caused by the \sim three-fold increase in $H_{\rm max}$, which pushes them radially outward.

Equation (16) implies $\nabla T \propto \nabla \rho^{\Gamma-1}$. Hence we expect thermal conduction to be less influential in model A $(\Gamma = 1.18)$ than in models B and C $(\Gamma = 5/3)$. The evolution of adiabatic model B (middle row of Fig. 6) is noticeably affected by the non-zero flux term F (cf. middle and right panels). The matter column near the pole has height $H_{\text{max}}(\theta \approx 0) = 1.8 \times 10^4 \text{ cm for } \mathbf{F} = 0 \text{ and}$ $H_{\text{max}}(\theta \approx 0) = 3.0 \times 10^4 \text{ cm for } \mathbf{F} \neq 0. \text{ Matter con-}$ centrates more at the base of the mountain $(r \approx R_{\rm in})$ for $F \neq 0$, reaching peak densities of $\rho_{\text{max}} = 6.8 \times 10^8 \text{ g cm}^{-3}$ for $\mathbf{F} = 0$ and $\rho_{\text{max}} = 9.2 \times 10^8 \text{ g cm}^{-3}$ for $\mathbf{F} \neq 0$ at $\theta=0.$ Both evolved mountains are denser than the initial state ($\rho_{\text{max}} = 6.4 \times 10^8 \text{ g cm}^{-3}$). Thermal conduction drives matter towards the pole, like what is seen in Fig. 5. The mountain grows taller, albeit comparatively less so than for model A, going from peak altitudes $H_{\rm max} \approx 4.0 \times 10^4$ cm to $H_{\rm max} \approx 4.2 \times 10^4 \text{ cm}$ with $\boldsymbol{F} = 0$ and $H_{\rm max} \approx 4.3 \times 10^4 \text{ cm}$ for $\mathbf{F} \neq 0$.

Adiabatic model C (bottom row of Fig. 6) evolves like model B. The mountain grows taller on the conduction time-scale, going from $H_{\rm max}\approx 4.0\times 10^3$ cm at t=0 to $H_{\rm max}\approx 5.0\times 10^3$ cm for ${\pmb F}=0$ and $H_{\rm max}\approx 5.3\times 10^3$ cm for ${\pmb F}\neq 0$. At t=0, the density maximum $\rho_{\rm max}=3.7\times 10^{11}$ g cm⁻³ lies at $r\approx R_{\rm in}$ and $\theta=0$. After evolution the density reaches maximum values at the same location of $\rho_{\rm max}=3.5\times 10^{11}$ g cm⁻³ ($\approx 5\%$ decrease) for ${\pmb F}=0$ and $\rho_{\rm max}=4.0\times 10^{11}$ g cm⁻³ ($\approx 8\%$ increase) for ${\pmb F}\neq 0$ at $t=2\tau_{\rm c}$. The compression of matter at the pole suggests that ${\pmb F}\neq 0$ acts to 'soften' the effective EOS.

By inspecting the magnetic field lines in Fig. 6, we see that $|\boldsymbol{B}|$ evolves similarly to ρ due to flux freezing. As discussed above, thermal conduction drives matter towards the pole, shifting \boldsymbol{B} accordingly (Payne & Melatos 2004; Priymak et al. 2011). Hence $|\boldsymbol{B}|$ decreases on the whole as time passes, most dramatically in the case of model C, which predicts $|\boldsymbol{B}|_{\text{max}} = 9.7 \times 10^{14}$ G at t = 0, $|\boldsymbol{B}|_{\text{max}} = 6.5 \times 10^{14}$ G for $\boldsymbol{F} = 0$ at $t = 2\tau_{\text{c}}$, and $|\boldsymbol{B}|_{\text{max}} = 6.6 \times 10^{14}$ G for $\boldsymbol{F} \neq 0$. This is similar to what occurs for the representative exam-

ple discussed in Sec. 3.1 and tests with different grid resolutions (not plotted), suggesting the possibility that $|B|_{\rm max}$ increases slightly for runs with conduction, independent of the EOS. Additional, higher-resolution convergence tests (cf. Appendix A) can be undertaken, if future observational applications warrant. The formation of dense filamentary regions $(\rho \sim 10^{-1} \rho_{\text{max}})$ for runs with $\mathbf{F} \neq 0$ at $\theta \approx 1.0$ causes several magnetic 'pockets' to form near the pole, as the magnetic field lines bend around poleward-drifting matter. The formation of filaments near the magnetic pole, as observed across all simulations with thermal conduction, may stem from thermal Parker-like instabilities (Parker 1953; Field 1965). These instabilities introduce 'finger-like' density structures, which emerge due to the propagation of contact discontinuities between lighter and denser sections of fluid (Stone & Gardiner 2007; Mouschovias et al. 2009). Although we only have one fluid in our model, the strong dependence of the conduction coefficient (19) on the local magnetic field strength, which varies strongly near the pole, may cause this 'fenced-off' behaviour. It has been shown that unstable modes grow faster in the presence of anisotropic thermal conduction (Lecoanet et al. 2012).

3.3 Heat flux

Figure 7 displays contours of temperature T (colour scale) and the direction of the thermal flux \mathbf{F} (arrows) extracted from the runs performed in Figure 6. We seek to identify the existence, and evolution, of thermal hot spots [e.g. Becker & Truemper (1997)].

The temperature varies gradually with r and θ for model A (top row), because the polytropic index Γ is nearly unity. Nevertheless, the maximum (at the pole) and minimum (at the mountain-atmosphere interface) values of Tare in the ratio $T_{\rm max}/T_{\rm min}\approx 10$, a significant contrast. The thermal flux is predominantly directed towards the base of the mountain at all times, but becomes more 'noisy' at large t, when local hot spots form. At $t=2\tau_c$ we see that the temperature profile becomes more uniform away from the pole, suggesting that the model evolves towards an isothermal end state $\left[d/dt\left(p/\rho\right)\approx0\right]$ for $t\gg\tau_{\rm c}$, even when thermal conduction is not implemented. At $\theta \approx 0.1$ for the run with $\mathbf{F} \neq 0$ (right panel) we see a region of relatively low temperature $(T_{\rm max}/T \sim 6)$ form. This 'heat sink' is underdense as seen in Fig. 6, and is surrounded by the local hot spots $(T_{\rm spots} \sim 5 \times 10^9 \text{ K})$ described above.

For Model B (middle row) we have $|F| \approx$ $10^{23} \text{ erg cm}^{-2} \text{s}^{-1}$, and \mathbf{F} is predominantly directed towards the pole at $\theta = 0$. In the run without conduction (middle panel) we see that F is almost indistinguishable from its t=0 counterpart except near the equator where heat flows into a hot column ($T \approx 6 \times 10^9$ K) at $\theta = 1.3$. The temperature evolves like the density, i.e. growing and spreading with ρ (cf. Fig. 6). When conduction is switched on, a hot region $(T \gtrsim 8 \times 10^9 \text{ K})$ forms near the pole which extends to the mountain-atmosphere interface at $H_{\rm max} \approx 4.2 \times 10^4$ cm. The flux is highest at the mountain-atmosphere interface and at altitude $r - R_{\rm in} \approx 1.3 \times 10^4$ cm. The flux is directed in different directions throughout the column, suggesting that localised hot spots form in the densest part of the mountain. Away from the pole ($\theta \gtrsim 0.1$), the heat flow is small $(|F| \lesssim 10^{-2} |F|_{\text{max}}).$

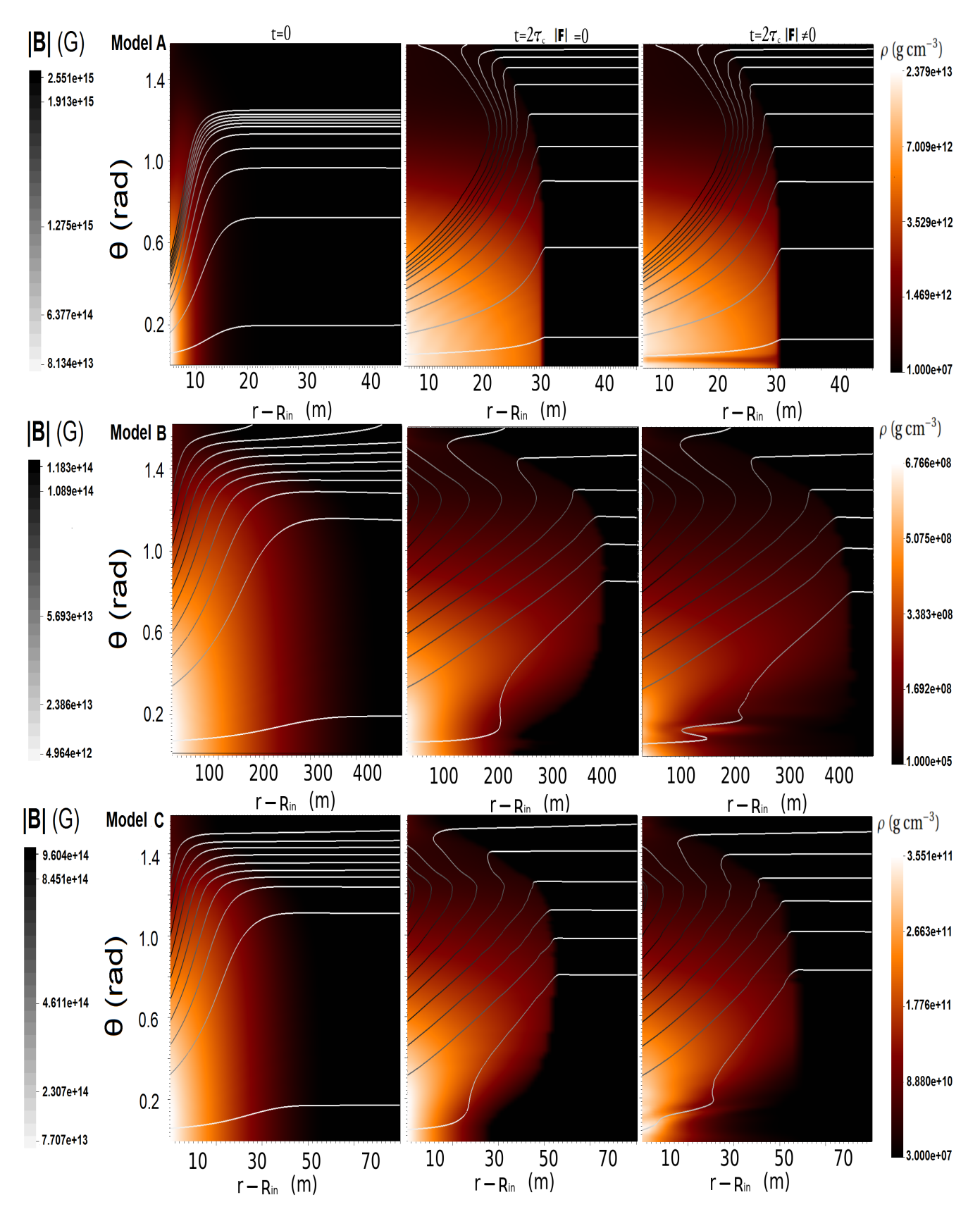


Figure 6. Density ρ (colour scale; brighter shades indicate higher ρ) and magnetic field lines (darker shades indicate higher $|\boldsymbol{B}|$) for a realistic accreted crust EOS (model A, top row; $M_a = 2.4 \times 10^{-5} M_{\odot} \approx 1.0 M_c$), and two idealised polytropic EOS (model B, middle row; $M_a = 3.0 \times 10^{-8} M_{\odot} \approx 1.2 M_c$; model C, bottom row; $M_a = 2.0 \times 10^{-6} M_{\odot} \approx 1.0 M_c$) studied by Priymak et al. (2011), at times t = 0 (left panel) and $t = 2\tau_c$ with $\boldsymbol{F} = 0$ (middle panel) and $t = 2\tau_c$ with $\boldsymbol{F} = 0$ (right panel). The fields are plotted as functions of altitude (horizontal axis) and colatitude (vertical axis).

In Model C (right panel) at t=0, we see that heat flows towards the pole $(|{\pmb F}|\approx 10^{21}~{\rm erg~cm^{-2}s^{-1}})$ and away from the equator $(|{\pmb F}|\approx 10^{20}~{\rm erg~cm^{-2}s^{-1}})$. At $t=2\tau_{\rm c}$, however, heat flows from the top of the mountain to the base near the equator $(\theta\approx 1.3)$, and little heat $(|{\pmb F}|\lesssim 10^{-4}|{\pmb F}|_{\rm max})$ flows near the pole, where a hot column $(T\approx 8\times 10^8~{\rm K})$ develops in a manner to similar to model B. Because of relation (16), the temperature profile evolves like the density and increases as the mountain grows $(T\propto \rho^{\Gamma-1})$; cf. Fig 6. Overall, the initially polytropic mountains respond similarly to thermal conduction by forming hot spots near the equator at $\theta\approx 1.3$ (models B and C) and near the pole at $\theta\approx 0.1$ (all models), where $|{\pmb F}|$ is largest.

4 GLOBAL OBSERVABLES

In this section we consider the evolution on the conduction time-scale $\tau_c \gg \tau_A$ (25) of the global observables μ (Sec. 4.1) and ϵ (Sec. 4.2) derived from runs of models A, B, and C. Simulations of mountains on the Alfvén time-scale τ_A have been performed previously using the codes ZEUS (Payne & Melatos 2007) and PLUTO (Mukherjee et al. 2013a,b).

4.1 Magnetic dipole moment

The theory of magnetic burial predicts that the global magnetic dipole moment for an axisymmetric mountain,

$$\mu = \frac{3r^4}{4} \int_{-1}^{1} d(\cos \theta) \cos \theta B_r(r, \theta), \tag{26}$$

evaluated at $r \gtrsim R_{\rm m}$, decreases as a function of M_a (Brown & Bildsten 1998; Melatos & Phinney 2001). In order to explore the relationship between burial, accreted mass, and thermal conduction for different EOS, we calculate μ from for a variety of PLUTO simulations with thermal conduction switched on.

Figure 8 shows how μ (normalized to the pre-accretion value μ_i) evolves due to thermal conduction for various accreted masses (0.1 $\leq M_a/M_c \leq 1$; left to right) and initially adiabatic EOS (1.18 $\leq \Gamma \leq 5/3$; top to bottom). Each panel displays $\mu(t)$ on a logarithmic temporal scale to capture both the MHD ($t \ll \tau_c$) and thermal ($t \gtrsim \tau_c$) dynamics. Again we emphasise that model A (top row of Fig. 8) corresponds most closely to an astrophysically realistic accreted crust. Models B and C are included for completeness to illustrate EOS-related trends and make contact with previous work (Priymak et al. 2011).

All the mountains depicted in Fig. 8 undergo an initially violent phase within $\lesssim 10^2 \tau_{\rm A}$, during which μ drops then rises. The behaviour observed in model A is similar to what is seen in Figures 6 and 14 of Vigelius & Melatos (2008) for example. It is largely driven by the MHD reconfiguration of the mountain rather than thermal conduction $(10^2 \tau_{\rm A} \ll \tau_{\rm c})$ (Vigelius & Melatos 2008; Mukherjee et al. 2013a). We find that μ decreases slightly for all mountains (maximum of $\approx 7\%$ for model A with $M_a/M_c \approx 0.2$), independent of the EOS, from t=0 to $t\sim 10^2 \tau_{\rm A}$, consistent with previous ZEUS simulations (Payne & Melatos 2007). Note that the Grad-Shafranov equilibria, and hence the evolution, are insensitive to the exact value of the initial dipole

moment μ_i provided that we have $M_a/M_c \lesssim 10$ [cf. the scaling law (1) introduced by Shibazaki et al. (1989)] (Payne & Melatos 2004, 2007). In this context, insensitive means that μ/μ_i depends on μ_i only through the ratio M_a/M_c and not on μ_i in isolation. Since Priymak et al. (2011) found that $M_c \propto \mu_i^2$, the insensitivity condition $M_a/M_c \lesssim 10$ translates into an EOS-dependent lower bound for μ_i . For the astrophysically relevant model A, we require [see expression (B26) of Priymak et al. (2011)]

$$\left(\frac{\mu_i}{3.2 \times 10^{30} \text{ G cm}^3}\right)^2 \gtrsim 0.4 \left(\frac{M_a}{10^{-4} M_{\odot}}\right) \left(\frac{R_{\star}}{10^6 \text{ cm}}\right)^6,$$
(27)

which is safely applicable to many LMXB systems, at least within the early stages of accretion (van den Heuvel & Bitzaraki 1995; Zhang & Kojima 2006). For $M_a/M_c \gtrsim 10$, the Grad-Shafranov modelling breaks down, and it is an open question whether the results are sensitive to μ_i or not.

On the longer time-scale $t\gtrsim \tau_c$, the behaviour of μ is qualitatively similar for all three initially polytropic EOS. In all cases, μ increases beyond μ_i ; runs with $M_a/M_c\gtrsim 0.1$ lead to $\mu(t\gtrsim \tau_c)>\mu(t=0)$. In effect thermal conduction resurrects some of the buried field, e.g. μ increases by $\approx 14\%$ in the case of model C with $M_a/M_c\approx 0.2$. For runs with $M_a/M_c\gtrsim 0.5$, μ increases significantly from its initial value at t=0, e.g. by up to $\approx 80\%$ in the case of model B for $M_a=3.0\times 10^{-8}M_{\odot}\approx 1.2M_c$.

For a realistic accreted crust (model A), we find $0.64 \le \mu/\mu_i \le 0.83$ for $0.2 \le M_a/M_c \le 1$ at $t=2\tau_c$. Small changes in μ for $t \gtrsim \tau_c$ in model A suggest that conduction plays a comparatively minor role in the evolution of astrophysically realistic mountains. Nevertheless we find that substantial $(\mu/\mu_i \lesssim 0.5)$ magnetic burial requires significantly greater accreted masses than previously estimated by Priymak et al. (2011); for example, $\mu(t=2\tau_c)/\mu(t=0)=1.28$ for $M_a/M_c(t=0)\approx 1$ suggests an increase in the characteristic mass M_c at $t=2\tau_c$ by a factor ~ 2 .

The inclusion of thermal conduction has the effect of partially resurrecting the buried field by increasing μ , which is similar to 'softening' the EOS [as found by Priymak et al. (2011)]. The comparatively small increase in μ for model A (see Fig. 8) implies that the realistic EOS softens less than for models B and C. This is expected because the polytropic index $\Gamma=1.18$ is closer to unity (i.e. nearly isothermal), implying that ∇T is smaller than for the isentropic gas models B and C.

4.2 Mass ellipticity

The characteristic gravitational wave strain emitted by a continuous-wave source is (Thorne 1980; Brady et al. 1998)

$$h_c = \left(\frac{128\pi^4}{15}\right)^{1/2} \frac{GI_{zz}\nu^2|\epsilon|}{dc^2},$$
 (28)

where I_{jk} is the moment-of-inertia tensor, ν is the spin frequency, d is the distance from the Earth to the source, and ϵ is the mass ellipticity,

$$\epsilon = \frac{I_{xx} - I_{yy}}{I_{zz}}. (29)$$

The magnitude of ϵ represents the primary uncertainty in estimating h_c in practical astrophysics applications [see e.g.

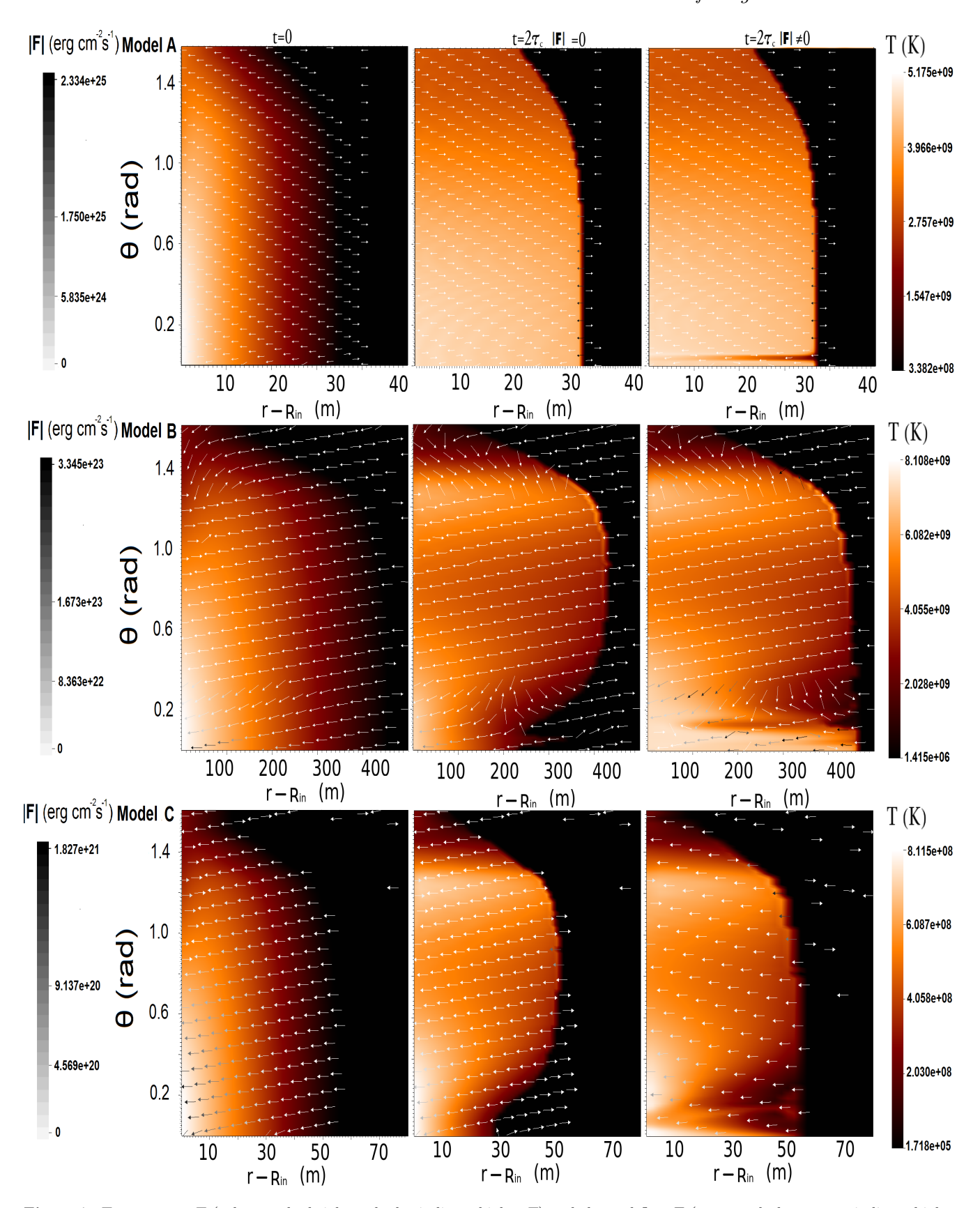


Figure 7. Temperature T (colour scale; brighter shades indicate higher T) and thermal flux \mathbf{F} (vectors; darker arrows indicate higher $|\mathbf{F}|$). The layout and simulation parameters are the same as in Fig. 6. Although the simulations in the middle column are run with $\mathbf{F} = 0$, we can still compare what a theoretical \mathbf{F} might be from (17), if conduction is switched on at some time t > 0.

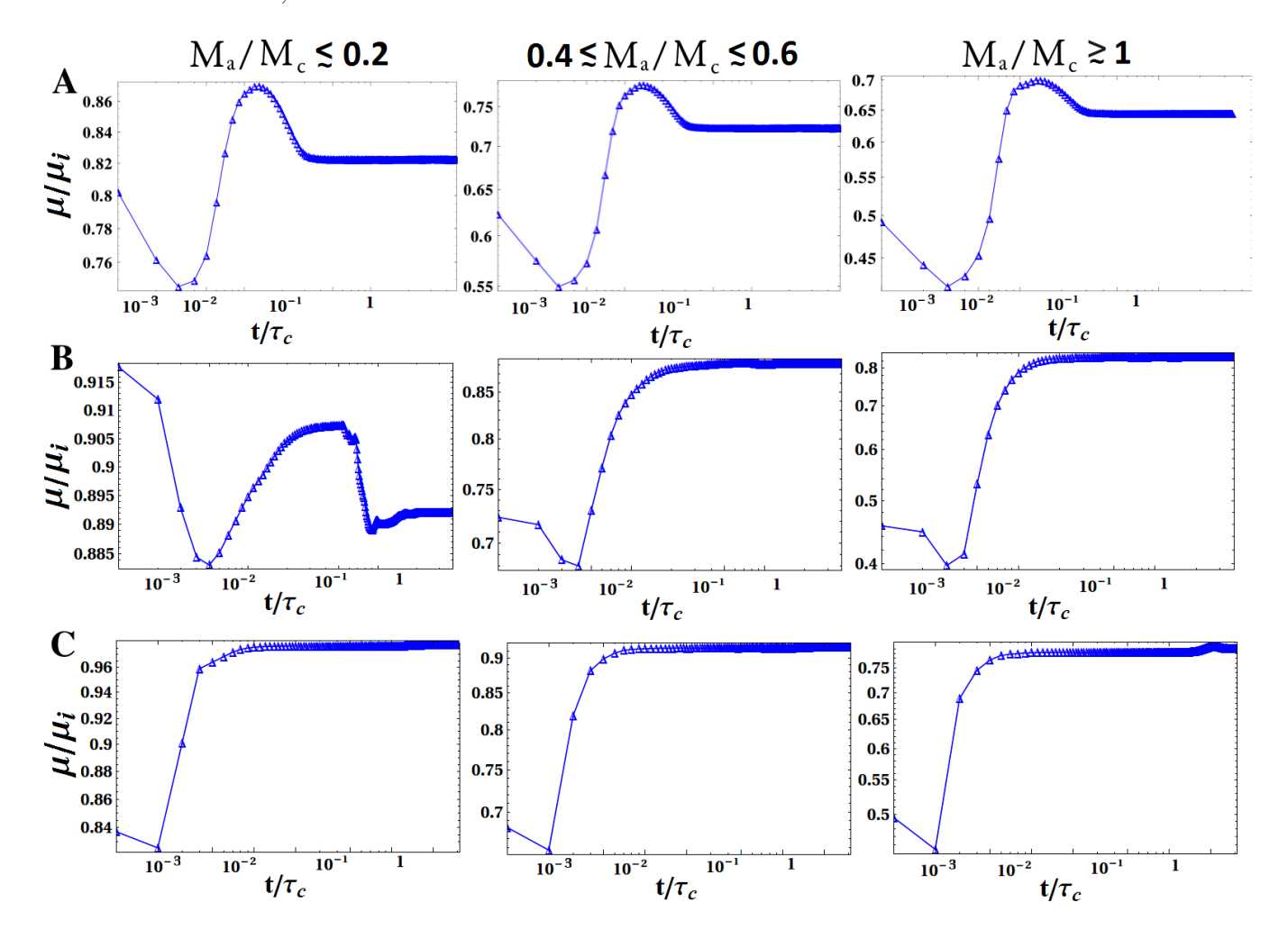


Figure 8. Evolution due to thermal conduction of the magnetic dipole moment μ [equation (26) evaluated at $r=R_{\rm m}$] normalised to the pre-accretion value μ_i for model A (top row) with accreted masses $M_a=1.2\times 10^{-5}M_{\odot}\approx 0.23M_c$ (left panel), $M_a=1.8\times 10^{-5}M_{\odot}\approx 0.58M_c$ (middle panel), and $M_a=2.4\times 10^{-5}M_{\odot}\approx 1.02M_c$ (right panel), model B (middle row) with $M_a=10^{-8}M_{\odot}\approx 0.09M_c$ (left panel), $M_a=2.0\times 10^{-8}M_{\odot}\approx 0.38M_c$ (middle panel), and $M_a=3.0\times 10^{-8}M_{\odot}\approx 1.18M_c$ (right panel), and model C with $M_a=1.0\times 10^{-6}M_{\odot}\approx 0.19M_c$ (left panel), $M_a=1.5\times 10^{-6}M_{\odot}\approx 0.47M_c$ (middle panel), and $M_a=2.0\times 10^{-6}M_{\odot}\approx 1.02M_c$ (right panel). Time is plotted in units of τ_c on a logarithmic scale to capture both the MHD ($t\ll \tau_c$) and thermal ($t\gtrsim \tau_c$) evolution.

Aasi et al. (2014); Mastrano et al. (2015); Suvorov et al. (2016b); though cf. Suvorov (2018)]. Here we can calculate ϵ directly from (29) using ρ as output by PLUTO. Thus we can explore the effects of thermal conduction on the detectability of magnetic mountains using ground-based interferometers such as the Laser Interferometer Gravitational-Wave Observatory (LIGO) (Harry & LIGO Scientific Collaboration 2010; Haskell et al. 2015).

Figure 9 plots ϵ against time (in units of τ_c) for different EOS and values of M_a . The layout is the same as in Fig. 8. All of the runs yield $\epsilon < 0$, indicating that the star is prolate⁵; the mountain is densest at the magnetic pole (Cutler 2002; Mastrano et al. 2011).

In contrast to the magnetic dipole moment (Sec. 4.1), $|\epsilon|$ increases with time for $t \gtrsim 10^2 \tau_{\rm A}$ for all runs with $M_a/M_c \gtrsim$

⁵ Since Vigelius & Melatos (2008) found that three-dimensional simulations of magnetic mountains relax to an almost axisymmetric state after a few Alfvén times (see Footnote 1), we expect the star to be prolate even without the assumption of axial symmetry.

0.1, by up to $\approx 45\%$ in the astrophysically realistic model A with $M_a/M_c \approx 1$. We also find smaller but still significant increases in $|\epsilon|$ in models B ($\approx 30\%$ with $M_a/M_c \approx 1$), and C ($\approx 27\%$ with $M_a/M_c \approx 1$). This result is consistent with the leading-order behaviour of ϵ given by (2), which implies that $|\epsilon|$ increases with M_c (Melatos & Payne 2005). As noted in Sec. 4.1, all runs display a \gtrsim two-fold increase in M_c at $t=2\tau_c$. Thermal conduction tends to facilitate the poleward drift of matter (see Sec. 3.2), thereby making the star more prolate.

The wobble angle of a precessing prolate star tends to grow, until the rotation and principal axes are orthogonal (Cutler 2002), which is the optimal state for gravitational wave emission. Hence, an accreting neutron star with a prolate magnetic mountain may be harder to detect than an isolated magnetar with the same $|\epsilon|$, which is oblate (Mastrano et al. 2011; Suvorov et al. 2016a). Note that, as discussed in Sec. 2.3, the values of $|\epsilon|$ presented in this section should be treated as upper limits since we do not model sinking (Wette et al. 2010).

A summary of simulation parameters and results is given in Table 3.

5 LONG-TERM THERMAL RELAXATION

In this section we explore the long-term thermal relaxation of a representative example of an astrophysically realistic mountain, namely model A with $M_a = 1.8 \times 10^{-5} M_{\odot} \approx$ $0.58M_c$. Long-term $(t \gg \tau_c)$ simulations face numerical difficulties because of the wide range of time-scales in the problem. For a typical mountain, maintaining a resolution of 128×128 grid points (see Appendix A) requires a time-step satisfying $\Delta t \lesssim 10^{-7} \tau_{\rm c}$ to avoid numerical instabilities. It is impractical to evolve the simulation for long times $(t \gg \tau_{\rm c})$. Lower-resolution runs (e.g. 64×64) fail catastrophically at $t \gtrsim \tau_{\rm c}$, because steep gradients are handled poorly at the now 'blurry' mountain-atmosphere interface; one ends up with $\rho < 0$ in places, for example. To circumvent these difficulties, we artificially increase the conduction coefficients κ_{\perp} and $\kappa_{||}$ to accelerate thermal relaxation; Vigelius & Melatos (2009b) took a similar approach to accelerate Ohmic decay. Increasing κ by a factor $\gtrsim 50$ causes the super-time-stepping algorithm to fail, when the parabolic Courant condition is eventually violated [see Appendix A and Alexiades et al. (1996)]. However, for an acceleration factor of \lesssim 50, the simulation is stable.

In order to increase the conductivities artificially, we set $\kappa_{\perp} \mapsto \xi \kappa_{\perp}$ and $\kappa_{||} \mapsto \xi \kappa_{||}$, where $1 \leqslant \xi \leqslant 40$ is a dimensionless constant. Equations (20) and (25) imply $\tau_c \approx 112/\xi$ s $\approx 5.6 \times 10^6 \tau_A/\xi$. Figures 10 and 11 display μ and ϵ respectively as functions of time for $\xi = 1, 10, 20, 30, 40$. To read the horizontal-axis for the $\xi = 30$ case, for example, a value on the axis of 10^{-1} implies that an interval lasting $t = 3\tau_c$ has effectively elapsed. The longest run effectively extends over the interval $0 \leqslant t \leqslant 80\tau_c$.

Both μ and $|\epsilon|$ increase with ξ . In other words, as κ_{\perp} and $\kappa_{||}$ increase, magnetic burial is mitigated, while the gravitational wave strain increases. Thermal conduction pushes matter towards the pole (as in Sec. 3.2 and Fig. 6). Increasing ${\pmb F}$ by a factor ξ amplifies polarward transport, i.e. ρ increases at the pole, as ξ increases, which is why $|\epsilon|$ increases with ξ and the star becomes more prolate. Increasing ρ near the pole effectively reduces the fraction $p/\rho^{\Gamma} = k_{\Gamma}$ there; i.e. increasing ξ can be thought of as reducing the effective polytropic constant and 'softening' the EOS by a factor related to ξ ; cf. Table 1. Hence, initially adiabatic mountains evolved with high \boldsymbol{F} come to resemble isothermal mountains at $t \gg \tau_{\rm c}$ [compare Fig. 10 with Figure 8 of Payne & Melatos (2004)]. For example, for $\xi = 40$, we have $\mu(t \gg \tau_c)/\mu_i = 0.73$, cf. $\mu(t = 0)/\mu_i = 0.63$. By comparison, we find $\mu/\mu_i = 0.73$ and $\mu/\mu_i = 0.63$ from isothermal Grad-Shafranov simulations (softest EOS) for $M_a \approx 10^{-5} M_{\odot}$ and $M_a \approx 10^{-4} M_{\odot}$ respectively. Comparing the $\xi = 1$ and $\xi = 40$ final states, we find that μ and ϵ differ by $\leq 3\%$ and $\leq 1\%$ respectively. The trends discussed above are also evident in simulations with different EOS and grid resolutions; see Appendix A.

We see that μ and ϵ continue to oscillate after $t \gtrsim 2\tau_{\rm c}$ albeit with small amplitude ($\lesssim 1\%$ peak to peak). The fluctuations at $t \gg \tau_{\rm c}$ persist, because some parts of the mountain take longer to settle down than others. In reality, heat

transport occurs more slowly than average in cold regions $(T_e \ll 10^8 \text{ K})$, meaning that conduction continues to affect cold parts of the mountain (whose effective conduction timescales are longer than the volume-averaged value τ_c), even after the rest of the mountain relaxes thermally. These cold regions, however, do not play a dominant role in determining μ or ϵ , as the density is low there.

6 CONCLUSIONS

In this paper we explore the effects of thermal conduction on the evolution of accretion-built mountains on neutron stars for time-scales $t \gtrsim \tau_{\rm c}$ (Secs. 3 and 4) and $t \gg \tau_{\rm c}$ (Sec. 5) using the MHD code PLUTO (Mignone et al. 2007). The initial states are generated from the Grad-Shafranov equation for a range of initially polytropic EOS documented in Table 1 (Payne & Melatos 2004; Priymak et al. 2011). Model A approximates a realistic, non-catalysed, accreted crust for densities in the range $10^8 \le \rho/\ \mathrm{g\ cm^{-3}} \le 10^{14}$ (Haensel & Zdunik 1990b). Models B and C approach the realistic EOS in the low- ρ and neutron drip density regimes respectively, and are included for completeness to illustrate EOS-related trends and make contact with previous work. The theory of magnetic burial predicts that, as matter piles up on the stellar surface, the dipole moment is reduced in accreting neutron stars in accord with the observed μ versus M_a relations, e.g. Taam & van den Heuvel (1986); van den Heuvel & Bitzaraki (1995). We find that thermal conduction has the effect of pushing accreted matter back towards the magnetic pole, where ∇T is greatest, thereby partially resurrecting the buried field and increasing μ while making the star more prolate. On the conduction time-scale, we find a quasi-static increase in the mountain's characteristic mass M_c [defined above equation (1)] starting from an adiabatic initial state. Hence achieving a given μ/μ_i value requires higher M_a , in general, than estimated by Priymak et al. (2011). The main trends are summarised in Table 3.

Gravitational radiation back-reaction can stall the spinup of the neutron star in a low-mass X-ray binary (LMXB) at hectohertz frequencies (Bildsten 1998), explaining the observation that LMXBs spin slower ($\nu_s \lesssim 650 \text{ Hz}$) than otherwise expected (Chakrabarty et al. 2003). The results in this paper suggest that the effective EOS of mountain matter may be softer than previously estimated, when thermal conductivity is included, leading to a proportionally higher gravitational wave strain (28). This strengthens the argument for targeting LMXBs such as Sco X-1 for searches with facilities like LIGO (Abbott et al. 2007; Riles 2013; Haskell et al. 2015). The increase in $|\epsilon|$ combined with the decrease in μ/μ_i at $t \gtrsim \tau_c$ for all runs with $M_a/M_c \gtrsim 0.1$ performed in this paper suggests that stars with significantly buried ($\mu \ll \mu_i$) magnetic fields may prove better gravitational wave candidates than previous estimates indicated (Melatos & Payne 2005; Priymak et al. 2011). However, we stress that the systematic and numerical (see Appendix A) uncertainties present within our models suggest that the effects of thermal conduction are likely to be small compared to other physical effects not implemented here, such as sinking (Wette et al. 2010).

In addition to searching for gravitational waves and measuring the global dipole moment, one can test the

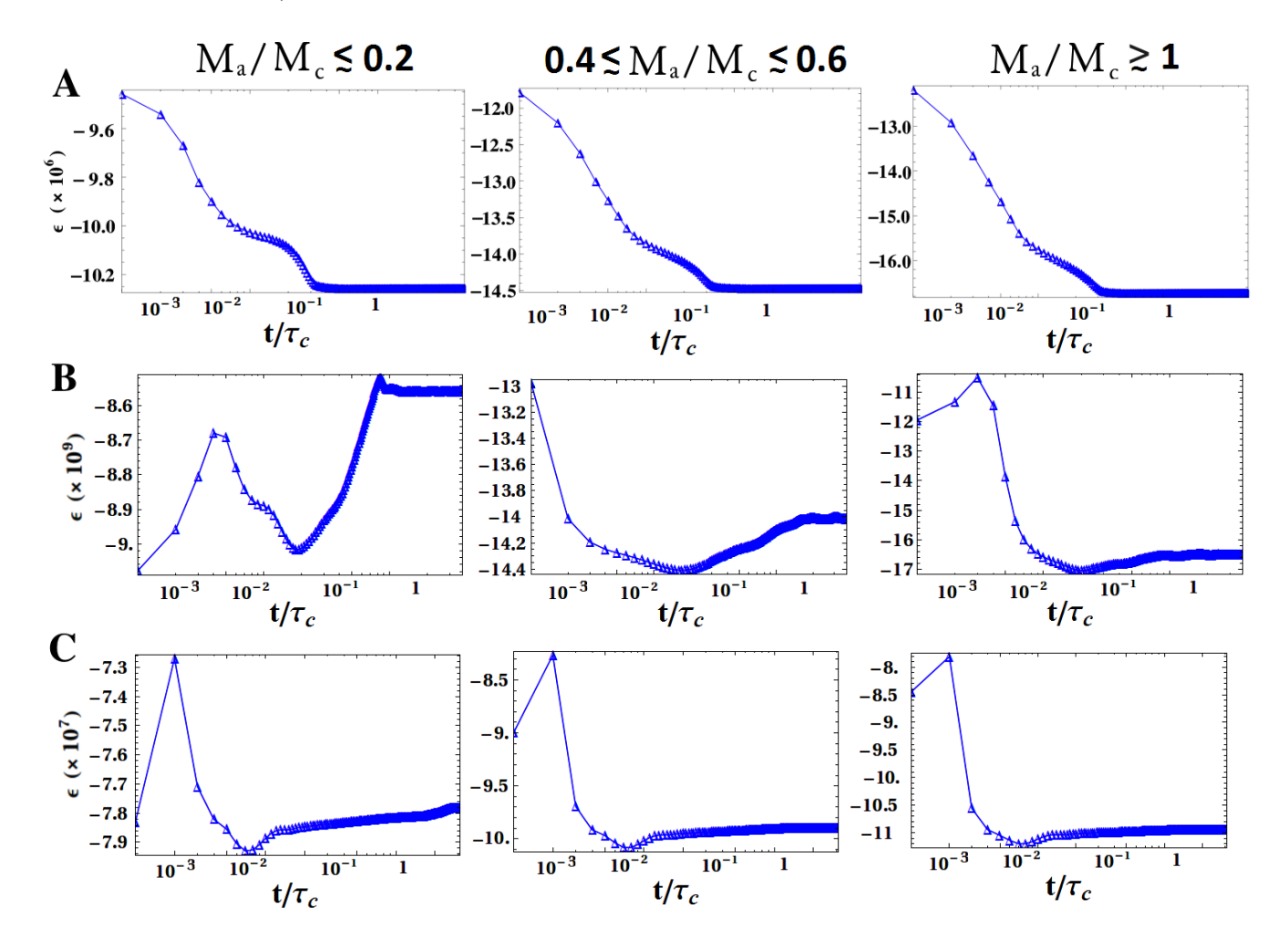


Figure 9. Evolution of the mass ellipticity ϵ evaluated from (29). The layout and simulation parameters are the same as in Fig. 8.

magnetic burial scenario by studying type I X-ray bursts (Strohmayer & Bildsten 2003; Cumming 2004; Payne & Melatos 2006b; Galloway et al. 2008). For adiabatic initial states, we find that mountains develop hot $(T \gtrsim 10^9 \text{ K})$ spots with large thermal fluxes near both the pole ($\theta = 0.1$) and the equator ($\theta = 1.3$) for a wide range of accreted masses (see Table 3 and Fig. 7). Dense filamentary regions also develop, especially for $M_a/M_c \gtrsim 1$. These effects cooperate to produce localized hot patches "fenced off" by intense magnetic fields, whose number increases with M_a [cf. Naravan & Heyl (2003)]. The hot spots may individually provide fuel for type I X-ray bursts which do not spread across the entire stellar surface, if the magnetic fences are intense enough to inhibit cross-field thermal transport (Keek et al. 2010; Misanovic et al. 2010). X-ray observations of significant heat fluxes near the magnetic pole of a neutron star in an LMXB, as broadly predicted by our simulations, may be related to the magnetic mountain physics (Narayan & Heyl 2003; Bhattacharyya & Strohmayer 2006; Cavecchi et al. 2017). Thermal fluxes out of the hot spots may also amplify shear stresses felt by the neutron star crust (Chugunov & Horowitz 2010; Beloborodov & Levin 2014). A detailed analysis of hotspot phenomena and their observational consequences will be conducted in future work. Another avenue to probe accretion mound physics comes from cyclotron features (Mukherjee & Bhattacharya 2012). Priymak et al. (2014) showed that one can discriminate, in principle, between magnetic mountain properties (e.g. EOS) by studying the line energy, width, and depth of theoretical cyclotron resonant scattering features from accreting neutron stars. These cyclotron features are, however, unlikely to be detected in the near future as it requires further development of sensitive X-ray polarimeters (Haskell et al. 2015).

ACKNOWLEDGMENTS

We thank Maxim Priymak and Donald Payne for permission to modify and use the Grad-Shafranov solver. We thank Dipanjan Mukherjee for expert instruction on the use of PLUTO. We thank HoChan Cheon for designing an early version of the script that converts Grad-Shafranov output into a format suitable for PLUTO input. We thank Patrick Clearwater, Brynmor Haskell, and Alpha Mastrano for discussions. We thank the anonymous referee for their carefully considered comments, and for providing the Skyrme EOS data used in Sec. 2.3 to estimate sinking depths. This work was supported in part by an Australian Postgraduate Award, the Albert Shimmins fund, and an Australian Research Council Discovery Project grant.

Table 3. Simulation parameters for $\mu_i = B_{\star} R_{\star}^3 \approx 3.2 \times 10^{30} \text{ G cm}^3$.

Time	$F \neq 0$ (yes/no)	EOS	$M_a \ (M_{\odot})$	μ/μ_i	$\begin{array}{c} \epsilon \\ (10^{-8}) \end{array}$	ρ_{max} (10 ⁹ g cm ⁻³)	$ {m B}_{ m max} \ (10^{12}{ m G})$
t = 0	_	A	1.2×10^{-5}	0.81	9.4×10^{2}	1.8×10^{4}	2.1×10^{3}
	_	A	1.8×10^{-5}	0.63	1.2×10^{3}	2.2×10^{4}	2.9×10^{3}
		A	2.4×10^{-5}	0.49	1.2×10^{3}	2.4×10^{4}	3.3×10^{3}
	_	В	1.0×10^{-8}	0.92	0.91	0.50	60
		В	2.0×10^{-8}	0.73	1.3	0.59	98
	_	В	3.0×10^{-8}	0.46	1.2	0.64	1.2×10^{2}
	_	$^{\rm C}$	1.0×10^{-6}	0.84	78	3.2×10^{2}	6.5×10^2
	_	$^{\rm C}$	1.5×10^{-6}	0.68	90	3.5×10^{2}	8.3×10^{2}
	_	$^{\mathrm{C}}$	2.0×10^{-6}	0.50	85	3.7×10^2	9.7×10^2
$t = 2\tau_{\rm c} \gg \tau_{\rm A}$	N	A	1.2×10^{-5}	0.75	1.0×10^{3}	1.1×10^{4}	1.3×10^{3}
	N	A	1.8×10^{-5}	0.60	1.4×10^{3}	1.2×10^{4}	1.9×10^{3}
	N	A	2.4×10^{-5}	0.44	1.5×10^3	1.4×10^{4}	2.0×10^3
	N	В	1.0×10^{-8}	0.86	0.83	0.53	50
	N	В	2.0×10^{-8}	0.77	1.3	0.61	68
	N	В	3.0×10^{-8}	0.55	1.5	0.68	78
	N	$^{\rm C}$	1.0×10^{-6}	0.91	76	3.1×10^{2}	5.0×10^{2}
	N	\mathbf{C}	1.5×10^{-6}	0.81	97	3.4×10^{2}	5.9×10^2
	N	$^{\rm C}$	2.0×10^{-6}	0.65	99	3.5×10^2	6.5×10^{2}
$t = 2\tau_{\rm c} \gg \tau_{\rm A}$	Y	A	1.2×10^{-5}	0.83	1.0×10^{3}	1.1×10^{4}	1.3×10^{3}
	Y	A	1.8×10^{-5}	0.73	1.5×10^{3}	1.3×10^{4}	2.0×10^{3}
	Y	A	2.4×10^{-5}	0.65	1.7×10^{3}	1.5×10^{4}	2.1×10^{3}
	Y	В	1.0×10^{-8}	0.89	0.85	0.89	51
	Y	В	2.0×10^{-8}	0.87	1.4	0.82	69
	Y	В	3.0×10^{-8}	0.81	1.7	0.90	79
	Y	\mathbf{C}	1.0×10^{-6}	0.97	78	3.5×10^2	5.1×10^2
	Y	$^{\rm C}$	1.5×10^{-6}	0.90	1.0×10^{2}	3.7×10^{2}	6.0×10^{2}
	Y	$^{\mathrm{C}}$	2.0×10^{-6}	0.77	1.1×10^2	4.0×10^2	6.6×10^2

REFERENCES

Aasi, J., Abadie, J., Abbott, B. P., et al. 2014, ApJ, 785, 119

Abbott, B., Abbott, R., Adhikari, R., et al. 2007, Physical Review D, 76, 082001

Akgün, T., Cerdá-Durán, P., Miralles, J. A., & Pons, J. A. 2018, MNRAS, 481, 5331

Alexiades, V., Amiez, G., & Gremaud, P. 1996, Com. Num. Meth. Eng., 12, 31

Alfvén, H. 1943, Arkiv for Astronomi, 29, 1

Arons, J. 1993, ApJ, 408, 160

Arzoumanian, Z., Chernoff, D. F., & Cordes, J. M. 2002, ApJ, 568, 289

Balbus, S. A. 1986, ApJ, 304, 787

Balescu, R. 1988, Transport Processes in a Plasma (Amsterdam: North-Holland)

Becker, W., & Truemper, J. 1997, A&A, 326, 682

Beckers, J. M. 1992, SIAM Journal on Numerical Analysis, $29,\,701$

Beloborodov, A. M., & Levin, Y. 2014, ApJL, 794, L24 Bhattacharyya, S., & Strohmayer, T. E. 2006, ApJL, 641, L53

Bildsten, L. 1998, ApJL, 501, L89

Bisnovatyi-Kogan, G. S., & Chechetkin, V. M. 1979, Soviet Physics Uspekhi, 22, 89

Blondin, J. M., & Freese, K. 1986, Nature, 323, 786

Brady, P. R., Creighton, T., Cutler, C., & Schutz, B. F. 1998, Physical Review D, 57, 2101

Braginskii, S. I. 1965, Reviews of Plasma Physics, 1, 205 Brown, E. F. 2000, ApJ, 531, 988

Brown, E. F., & Bildsten, L. 1998, ApJ, 496, 915

Brown, E. F., Bildsten, L., & Rutledge, R. E. 1998, ApJL, $504,\, \mathrm{L95}$

Čada, M., & Torrilhon, M. 2009, Journal of Computational Physics, 228, 4118

Cavecchi, Y., Watts, A. L., & Galloway, D. K. 2017, ApJ, 851, 1

Chakrabarty, D., Morgan, E. H., Muno, M. P., et al. 2003, Nature, 424, 42

Chamel, N., & Haensel, P. 2008, Living Reviews in Relativity, 11, 10

Chamel, N., Fantina, A. F., Zdunik, J. L., & Haensel, P. 2015, Physical Review C, 91, 055803

Chandrasekhar, S. 1956, ApJ, 124, 232

Chandrasekhar, S. 1967, New York: Dover, 1967,

Chugunov, A. I., & Horowitz, C. J. 2010, MNRAS, 407, L54

Courant, R., & Hilbert, D. 1953, Methods of Mathematical Physics, Vol. I (New York: Interscience Publication)

Cumming, A. 2004, IAU Colloq. 190: Magnetic Cataclysmic Variables, 315, 58

Cumming, A., Zweibel, E., & Bildsten, L. 2001, ApJ, 557, 958

Cutler, C. 2002, Physical Review D, 66, 084025

Douchin, F., & Haensel, P. 2001, A&A, 380, 151

Faucher-Giguère, C. A., & Kaspi, V. M. 2006, ApJ, 643, 332

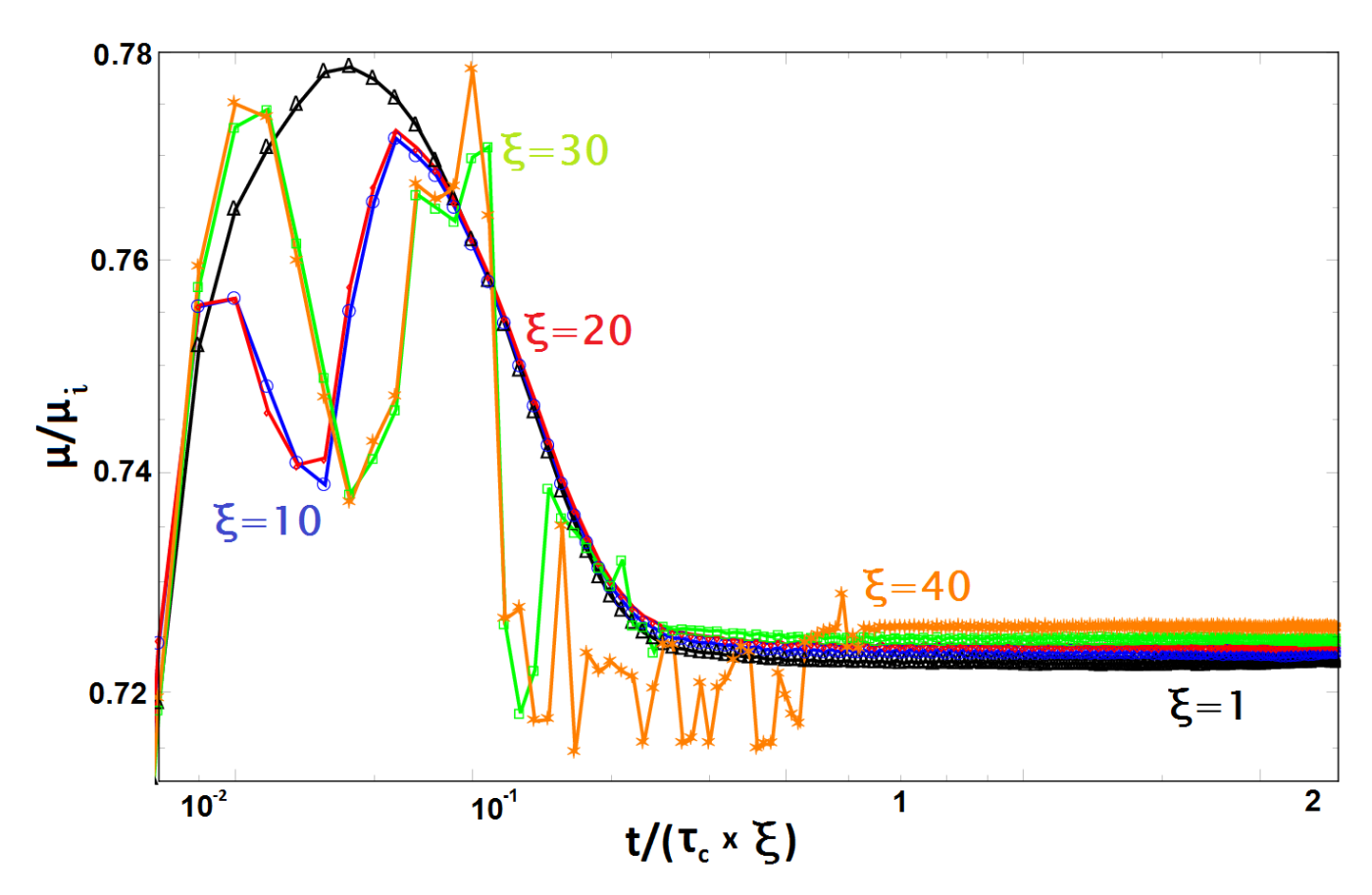


Figure 10. Magnetic dipole moment μ (normalised to the pre-accretion value μ_i) as a function of time for model A with $M_a=1.8\times 10^{-5}M_{\odot}\approx 0.58M_c$ and thermal conduction switched on. The conductivites κ_{\perp} and $\kappa_{||}$ are artificially rescaled according to $\xi\kappa_{\perp}$ and $\xi\kappa_{||}$ for $\xi=1$ (black, triangles), $\xi=10$ (blue, circles), $\xi=20$ (red, diamonds), $\xi=30$ (green, squares), and $\xi=40$ (orange, stars). The horizontal axis is also rescaled by expressing time in units of $\xi\tau_c$.

 $Field,\,G.\,\,B.\,\,1965,\,ApJ,\,142,\,531$

Fujimoto, M. Y., Hanawa, T., Iben, I., Jr., & Richardson, M. B. 1984, ApJ, 278, 813

Galloway, D. K., Muno, M. P., Hartman, J. M., Psaltis, D., & Chakrabarty, D. 2008, The Astrophysical Journal Supplement, 179, 360-422

Galloway, D. K., Premachandra, S., Steeghs, D., et al. 2014, ApJ, 781, 14

Gardiner, T. A., & Stone, J. M. 2005, Journal of Computational Physics, 205, 509

Geppert, U., & Viganò, D. 2014, MNRAS, 444, 3198

Glampedakis, K., & Andersson, N. 2006, Physical Review D, 74, 044040

Goldreich, P., & Reisenegger, A. 1992, ApJ, 395, 250

Harry, G. M., & LIGO Scientific Collaboration 2010, Classical and Quantum Gravity, 27, 084006

Haskell, B., Jones, D. I., & Andersson, N. 2006, MNRAS, 373, 1423

Haskell, B., Priymak, M., Patruno, A., et al. 2015, MN-RAS, 450, 2393

Haensel, P., & Zdunik, J. L. 1990, A&A, 227, 431

Haensel, P., & Zdunik, J. L. 1990, A&A, 229, 117

van den Heuvel, E. P. J., & Bitzaraki, O. 1995, A&A, 297, L41

Johnson-McDaniel, N. K., & Owen, B. J. 2013, Physical Review D, 88, 044004 Keek, L., Galloway, D. K., in't Zand, J. J. M., & Heger, A. 2010, ApJ, 718, 292

Klimchuk, J. A., & Sturrock, P. A. 1989, ApJ, 345, 1034Konar, S., & Choudhuri, A. R. 2002, Bulletin of the Astronomical Society of India, 30, 697

Konar, S., & Choudhuri, A. R. 2004, MNRAS, 348, 661Konar, S. 2010, MNRAS, 409, 259

Kosiński, R., & Hanasz, M. 2006, Astronomische Nachrichten, 327, 479

Kundu, P. K., & Cohen, I. M. 2008, Fluid Mechanics: Fourth Edition (London, England: Academic Press)

Landau, L. D., & Lifshitz, E. M. 1959, Fluid Mechanics (Oxford: Pergamon Press)

Lasky, P. D. 2015, PASA, 32, e034

Lecoanet, D., Parrish, I. J., & Quataert, E. 2012, MNRAS, 423, 1866

Litwin, C., Brown, E. F., & Rosner, R. 2001, ApJ, 553, 788 Mackie, F. D., & Baym, G. 1977, Nuclear Physics A, 285, 332

Mastrano, A., Melatos, A., Reisenegger, A., & Akgün, T. 2011, MNRAS, 417, 2288

Mastrano, A., & Melatos, A. 2012, MNRAS, 421, 760 Mastrano, A., Suvorov, A. G., & Melatos, A. 2015, MN-RAS, 447, 3475

Melatos, A., & Payne, D. J. B. 2005, ApJ, 623, 1044 Melatos, A., & Phinney, E. S. 2001, PASA, 18, 421

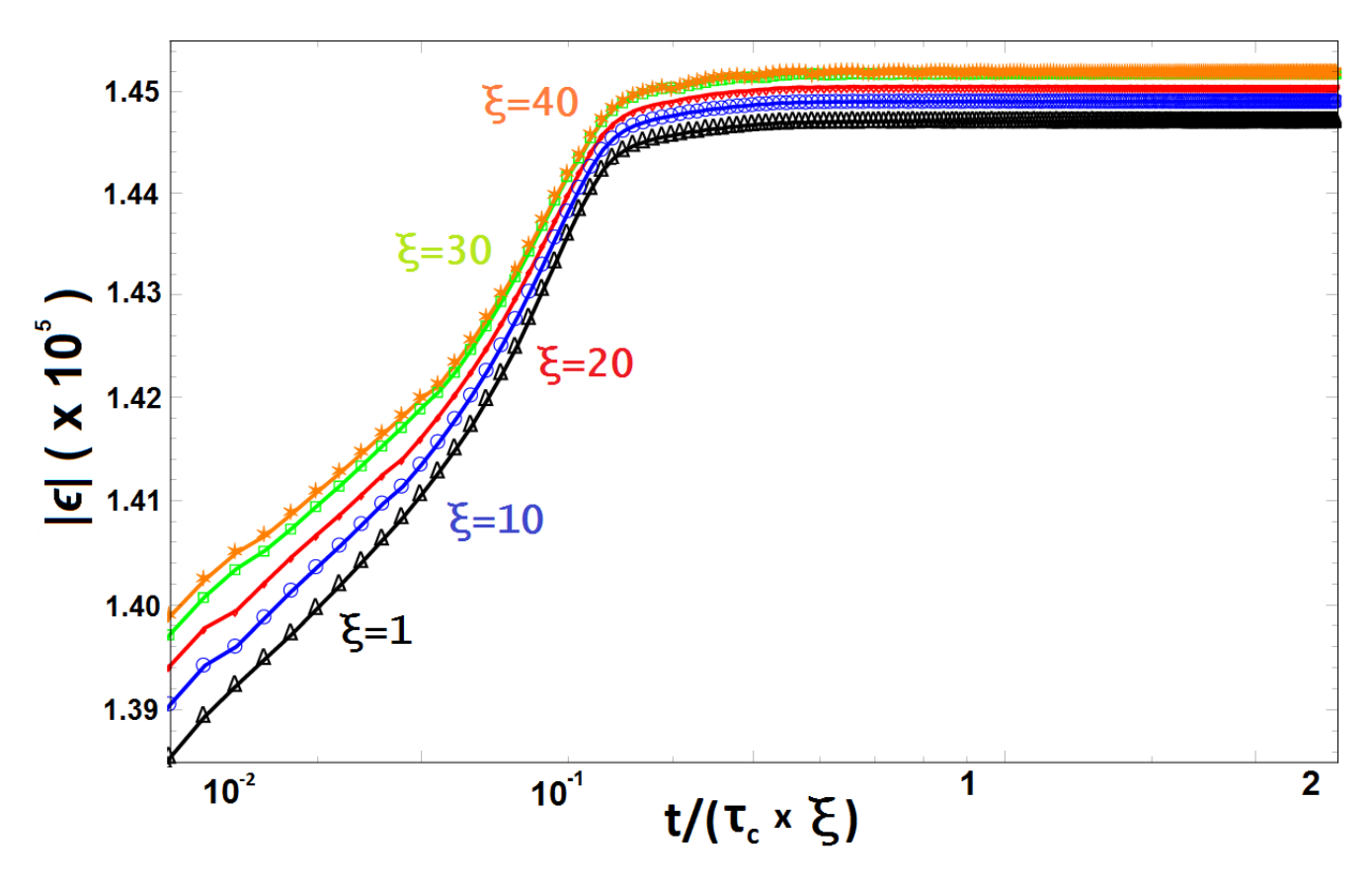


Figure 11. Ellipticity ϵ [equation (29)] for the simulation parameters in Fig. 10. Note that ϵ is negative.

Mignone, A., Bodo, G., Massaglia, S., et al. 2007, The Astrophysical Journal Supplement, 170, 228

Mignone, A., & Tzeferacos, P. 2010, Journal of Computational Physics, 229, 2117

Miralda-Escude, J., Paczynski, B., & Haensel, P. 1990, ApJ, 362, 572

Misanovic, Z., Galloway, D. K., & Cooper, R. L. 2010, ApJ, 718, 947

Miyoshi, T., & Kusano, K. 2005, Journal of Computational Physics, 208, 315

Mouschovias, T. C. 1974, ApJ, 192, 37

Mouschovias, T. C., Kunz, M. W., & Christie, D. A. 2009, MNRAS, 397, 14

Mukherjee, D., & Bhattacharya, D. 2012, MNRAS, 420, 720

Mukherjee, D., Bhattacharya, D., & Mignone, A. 2013, MNRAS, 430, 1976

Mukherjee, D., Bhattacharya, D., & Mignone, A. 2013, MNRAS, 435, 718

Narayan, R., & Heyl, J. S. 2003, ApJ, 599, 419

Nishimura, O. 2005, Publications of the Astronomical Society of Japan, 57, 769

Parker, E. N. 1953, ApJ, 117, 431

Patruno, A. 2012, ApJL, 753, L12

Payne, D. J. B., & Melatos, A. 2004, MNRAS, 351, 569

Payne, D. J. B., & Melatos, A. 2006, ApJ, 641, 471

Payne, D. J. B., & Melatos, A. 2006, ApJ, 652, 597

Payne, D. J. B., & Melatos, A. 2007, MNRAS, 376, 609

Potekhin, A. Y. 1999, A&A, 351, 787

Potekhin, A. Y., Fantina, A. F., Chamel, N., Pearson, J. M., & Goriely, S. 2013, A&A, 560, A48

Press, W. H., Flannery, B. P., & Teukolsky, S. A. 1986, Cambridge: University Press, 1986,

Priymak, M., Melatos, A., & Lasky, P. D. 2014, MNRAS, $445,\,2710$

Priymak, M., Melatos, A., & Payne, D. J. B. 2011, MN-RAS, 417, 2696

Riles, K. 2013, Progress in Particle and Nuclear Physics, 68, 1

Sato, K. 1979, Progress of Theoretical Physics, 62, 957

Schatz, H., Bildsten, L., Cumming, A., & Wiescher, M. 1999, ApJ, 524, 1014

Shapiro, S. L., & Teukolsky, S. A. 1983, Black holes, white dwarfs, and neutron stars: The physics of compact objects (New York: Wiley-Interscience)

Shibazaki, N., Murakami, T., Shaham, J., & Nomoto, K. 1989, Nature, 342, 656

Srinivasan, G., Bhattacharya, D., Muslimov, A. G., & Tsygan, A. J. 1990, Current Science, 59, 31

Stone, J. M., & Gardiner, T. 2007, ApJ, 671, 1726

Strohmayer, T., & Bildsten, L. 2006, Cambridge Astrophysics Series, 39, 113

Suvorov, A. G., Mastrano, A., & Melatos, A. 2016, MN-RAS, 456, 731

Suvorov, A. G., Mastrano, A., & Geppert, U. 2016, MN-RAS, 459, 3407

Suvorov, A. G. 2018, Physical Review D, 98, 084026

Taam, R. E., & van den Heuvel, E. P. J. 1986, ApJ, 305,

235

Thorne, K. S. 1980, Reviews of Modern Physics, 52, 299 Urpin, V., & Geppert, U. 1995, MNRAS, 275, 1117 Ushomirsky, G., Cutler, C., & Bildsten, L. 2000, MNRAS, 319, 902

Vigelius, M., & Melatos, A. 2008, MNRAS, 386, 1294
Vigelius, M., & Melatos, A. 2009, MNRAS, 395, 1963
Vigelius, M., & Melatos, A. 2009, MNRAS, 395, 1985
Vigelius, M., & Melatos, A. 2009, MNRAS, 395, 1972
Wang, J., Zhang, C. M., & Chang, H.-K. 2012, A&A, 540, A100

Wette, K., Vigelius, M., & Melatos, A. 2010, MNRAS, 402, 1099

Yoshida, S. 2013, MNRAS, 435, 893

Zdunik, J. L., Haensel, P., Paczynski, B., & Miralda-Escude, J. 1992, ApJ, 384, 129

Zhang, C. M., & Kojima, Y. 2006, MNRAS, 366, 137

APPENDIX A: PLUTO SIMULATIONS

Complete documentation for the PLUTO code was published by Mignone et al. (2007). The specific features we rely upon and optimize are discussed below.

Grid and time step

We employ a static, two-dimensional, polar grid with $N_r \times N_\theta = 128 \times 128$ grid points. The radial grid comprises a logarithmic section with 100 points for $R_{\rm in} \leqslant r \leqslant 2R_{\rm mountain}$, and a uniform section with 28 points for $2R_{\rm mountain} \leqslant r \leqslant R_{\rm m}$, where $R_{\rm mountain}$ is defined arbitrarily at t=0 as the innermost radial grid point with $\rho \leqslant 10^{-7} \rho_{\rm max}$. A mixed grid captures features with sharply different length-scales and minimizes the interpolation errors discussed in Sec. 3. We find that including additional grid points in the atmosphere $(R_{\rm mountain} \leqslant r \leqslant R_{\rm m})$ increases the computational cost without modifying perceptibly the observables computed in Sec. 4. The angular grid is uniformly spaced in θ over $0 \leqslant \theta \leqslant \pi/2$.

We employ a Runge-Kutta third-order time-stepper for safety, although we find by experimentation that the results are essentially indistinguishable from the second-order variant. We employ the third-order finite-volume spatial integrator 'Lim03' to interpolate between grid points (Čada & Torrilhon 2009). This scheme resolves local minima with high precision, e.g. strong gradients at the mountain-atmosphere interface. We use a time-step $\Delta t = 5 \times 10^{-8} \tau_{\rm c}$ where $\tau_{\rm c}$ is determined through equation (25). We print output files at various fractions of $\tau_{\rm c}$ depending on the specifics of the run; cf. the horizontal-axes on Figs. 8 and 9. This Δt is small enough to avoid Courant-Friedrichs-Lewy (CFL) instabilities for each run.

In order to avoid numerical instabilities we simulate the mountain together with an atmosphere which has a small but non-zero density taken as $\rho_{\rm atm}=10^{-8}\rho_{\rm max}$. The atmosphere alleviates numerical difficulties associated with strong gradients and prevents the density from dipping below zero due to numerical fluctuations. We find that varying $\rho_{\rm atm}$ in the range $10^{-9} \leqslant \rho_{\rm atm}/\rho_{\rm max} \leqslant 10^{-5}$ does not modify the observables discussed in Sec. 3 and 4 by more than

 $\sim 1\%$. The code crashes for $\rho_{\rm atm} \lesssim 10^{-9} \rho_{\rm max}$, because ρ dips below zero somewhere unless we set $\Delta t \lesssim 10^{-11} \tau_{\rm c}$, which is too expensive computationally. We define a flag that sets $\max(\rho, \rho_{\rm atm}) \mapsto \rho$ at every grid point after each time step Δt so that the atmosphere has a minimum density of $\rho_{\rm atm}$ for all t.

We find that the bilinear interpolation algorithm of PLUTO introduces errors of $\leq 1\%$ in the quantities calculated in Secs. 3 and 4 between the t=0 (grid-realigned) PLUTO output and the raw Grad-Shafranov data; cf. Figures 2 and 4 of Priymak et al. (2011) with Figs. 8 and 9.

Divergence cleaning and thermal conduction

Maxwell's equations require $\nabla \cdot \boldsymbol{B} = 0$ at all times. Various strategies can be employed to minimise numerical deviations from $\nabla \cdot \boldsymbol{B} = 0$. For example, the extended hyperbolic divergence cleaning algorithm (Mignone & Tzeferacos 2010) introduces Lagrange multipliers into Faraday's law (12). Inspection of PLUTO output files confirms that $\nabla \cdot \boldsymbol{B}$ vanishes to floating-point precision as a consequence of using this algorithm. The divergence cleaning algorithm is coupled with the approximate Riemann solver 'hlld' designed to resolve shocks and strong gradient phenomena (Miyoshi & Kusano 2005).

Thermal conduction (see Sec. 3) is implemented via the super-time-stepping algorithm available in PLUTO and described in Alexiades et al. (1996). The energy equation (13) has a parabolic Courant number C_p associated with it, which depends on the value of the conduction coefficients $\kappa_{||}$ and κ_{\perp} . Together with the usual Courant number condition (Landau & Lifshitz 1959), we require $C_p \leq 1/N_{\text{dim}} = 1/2$ to avoid instabilities (Beckers 1992). Super-time-stepping allows for flux terms to be treated in a separate 'super-step' using operator splitting methods, so that Δt need not be reduced to avoid parabolic CFL instabilities.

Implementation, stability, and convergence tests

We test our PLUTO simulations in four ways. For implementation: (i) We compute the total mass of the simulation at each time-step to check for mass leakage. (ii) We check the surface dipole moment and the velocity field to ensure that the boundary conditions described in Sec. 2.2 are implemented faithfully. For convergence: (iii) We vary the grid parameters N_r and N_θ to check if the results depend on the spatial resolution (see Figs. A1 and A2). For stability: (iv) We vary the super-time-stepping parameters, the CFL parameters, and the thermal conduction coefficients (i.e. checking if the conduction and no-conduction runs match smoothly in the limit $\kappa \to 0$). The convergence of the Grad-Shafranov code described in Sec. 2.2 is studied fully by Payne & Melatos (2004) and Priymak et al. (2011).

In Figures A1 and A2 we show the evolution of the ellipticity and dipole moment, respectively, for model B with $M_a = 2 \times 10^{-8} M_{\odot}$ and thermal conduction switched on, with $N_r \times N_{\theta} = 96 \times 96$ grid points and varying values of ξ (this parameter is introduced to artificially scale the conduction coefficients, see Sec. 5). Two major points are evident from these plots. First, the trends associated with increasing ξ for model B are the same as was observed for model

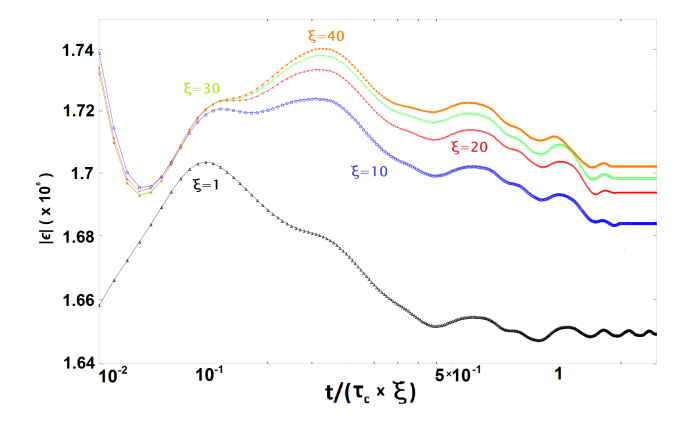


Figure A1. Evolution of ϵ for model B with $M_a = 2 \times 10^{-8} M_{\odot}$ with 96 × 96 grid points for $\xi = 1$ (black, triangles), $\xi = 10$ (blue, circles), $\xi = 20$ (red, diamonds), $\xi = 30$ (green, squares), and $\xi = 40$ (orange, stars).

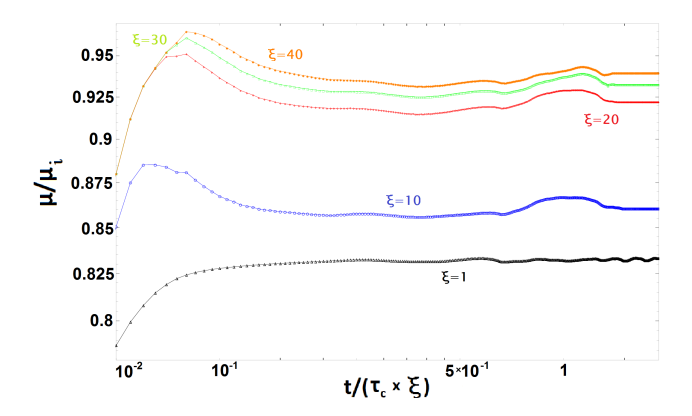


Figure A2. Evolution of μ for model B with $M_a=2\times 10^{-8}M_{\odot}$ with 96×96 grid points for $\xi=1$ (black, triangles), $\xi=10$ (blue, circles), $\xi=20$ (red, diamonds), $\xi=30$ (green, squares), and $\xi=40$ (orange, stars).

A in Sec. 5; $|\epsilon|$ and μ/μ_i are monotonically increasing with increasing values of ξ at $t\gtrsim \tau_c$, independent of the EOS and grid resolution. The second point concerns the convergence test (iii) detailed above: for the $\xi=1$ run (black, diamonds), all simulation parameters are identical to those for the simulations performed in Sec. 4 for the same accreted mass and EOS (middle figure of the middle panel), except that the resolution is lower for the runs presented here. Comparing the final ellipticity and μ values from Figs. A1 and A2 with those presented in Table 3 for the higher resolution run, we see only a small ($\lesssim 10\%$) disparity at late times, with $\epsilon(96\times96)=1.65\times10^{-8}$, $\epsilon(128\times128)=1.44\times10^{-8}$, $\mu(96\times96)/\mu_i=0.83$, and $\mu(128\times128)/\mu_i=0.87$.

Figure A3 plots the total mass as a function of time without (black, triangles) and with (blue, circles) thermal conduction for model B with $M_a = 2 \times 10^{-8} M_{\odot}$. We see that, after an initial adjustment phase, the total mass returns to M_a within $\sim 3\%$ ($\sim 4\%$) without (with) thermal conduction. This adjustment phase ($t \ll \tau_c$) occurs for two separate reasons. The first is due to the artificial atmospheric density $\rho_{\rm atm} = 10^{-8} \rho_{\rm max}$, introduced to ensure that the simulation does not produce $\rho < 0$ at any point throughout the evolution. Some of this atmospheric mass actually gets pulled

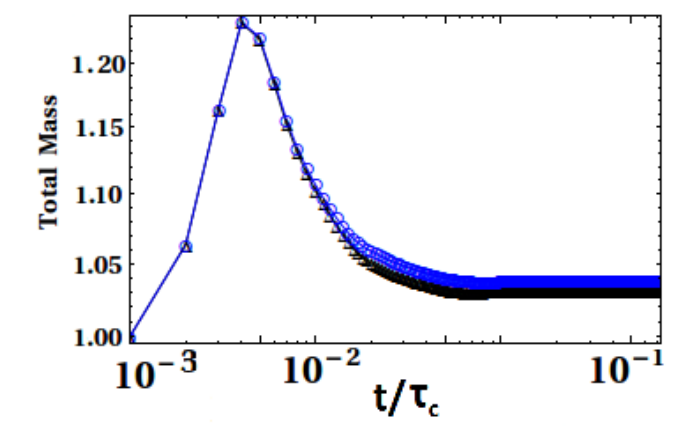


Figure A3. Total mass enclosed in the simulation box (in units of M_a) as a function of time for model B with $M_a = 2 \times 10^{-8} M_{\odot}$, evolved with (blue, circles) and without (black, triangles) thermal conduction.

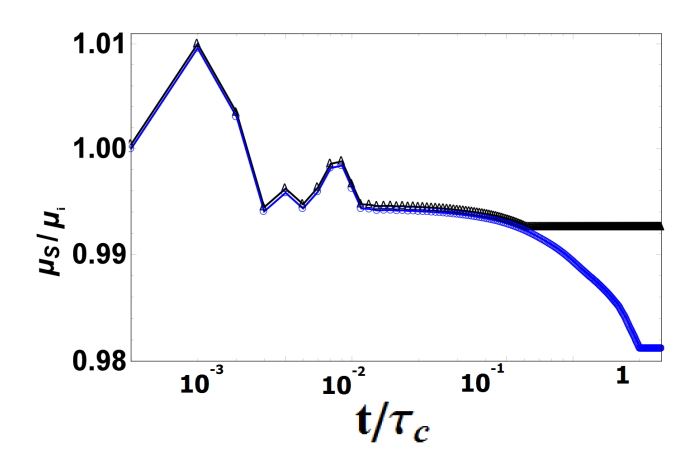


Figure A4. Surface magnetic dipole moment $\mu_{\rm S}$ [equation (26) evaluated at $r=R_{\rm in}$] as a function of time, normalised to the pre-accretion value μ_i for model A with $M_a=1.8\times 10^{-5}M_{\odot}$, evolved with (blue, circles) and without (black, triangles) thermal conduction.

down into the mountain, after which the atmosphere resets, thus increasing the overall mass of the simulation slightly. Additionally, the Grad-Shafranov equilibria are defined over grids which are slightly different to those in PLUTO. Hence, at t=0, the MHD equations are not exactly satisfied in PLUTO, leading to a temporary increase in the total mass. These two effects combine to increase the total mass in the initial stages of evolution. Table A2 in Payne & Melatos (2007) reports similar total mass changes during the adjustment phase. Figure A3 is typical for runs performed in this paper.

In Figure A4 we plot the surface dipole moment $\mu_{\rm S}$ [equation (26) evaluated at $r=R_{\rm in}$] as a function of time without (black, triangles) and with (blue, circles) thermal conduction for model A with $M_a=1.8\times 10^{-5}M_{\odot}$. If the boundary conditions at the stellar surface [namely $\psi(R_{\rm in},\theta)=\psi_{\star}\sin^2\theta$] are implemented without numerical error, $\mu_{\rm S}$ should keep its initial value μ_i . We see a slight variation (maximum of $\sim 2\%$). Figure A4 is typical for runs performed in this paper.

APPENDIX B: IDEAL-GAS APPROXIMATION TO THE EQUATION OF STATE

Strictly speaking, the accreted matter in the crust is partially degenerate (Schatz et al. 1999). In this appendix, we verify that it is reasonable to approximate the EOS by the ideal-gas formula (16), for ease of use in PLUTO, when calculating the perturbations to the mountain structure caused by thermal transport. The equilibrium configuration of the mountain before thermal transport is switched on is calculated for the full, degenerate, polytropic EOS (see Sec. 2).

In a Fermi-Dirac distribution, the mean occupancy n for a single-particle orbital with energy E is given by

$$n(E) = \frac{1}{\exp\left[\frac{E - \sigma}{k_B T}\right] + 1},\tag{B1}$$

where σ is the chemical potential, which is a function of ρ and T (in general). In the limit $T \to 0$, n(E) tends to either 1 or 0 for $E < \sigma$ or $E > \sigma$, respectively. The Fermi temperature T_F is defined through the chemical potential via

$$\sigma = k_B T_F. \tag{B2}$$

The dependence of σ on ρ and T is determined by integrating the mean occupancy to obtain the total particle number,

$$N = \int_0^\infty n(E)D(E)dE,$$
 (B3)

where D(E) is the density of states.

The pressure p is defined via the first law of thermodynamics, viz.

$$p = -\frac{(T - \varepsilon S - \sigma N)}{V},\tag{B4}$$

where ε and S denote the internal energy and entropy, respectively, and -pV is the grand canonical potential. Substituting (B4) into the integral (B1) allows one to express T in terms of p and ρ for $T \neq 0$, i.e. defines the EOS. One finds

$$\frac{pm}{\rho k_B T} = \frac{\mathcal{F}(5/2, z)}{\mathcal{F}(3/2, z)},\tag{B5}$$

for an arbitrary Fermi gas, with

$$\mathcal{F}(\nu, z) = \frac{1}{\Gamma(\nu)} \int_0^\infty \frac{x^{\nu - 1}}{z^{-1} e^x + 1} dx,$$
 (B6)

and fugacity $z = \exp(\sigma/k_B T)$ [see e.g. Shapiro & Teukolsky (1983) for details]. Expression (B5) is plotted in Fig. B1.

In regions with $T \gg T_F$, expression (B5) approaches the ideal gas law (16),

$$p \propto \rho k_B T.$$
 (B7)

In regions with $T \ll T_F$, expression (B5) approaches a polytropic EOS (Chandrasekhar 1967),

$$p \propto \rho^{5/3}$$
. (B8)

An accurate description of a realistic accreted crust lies between these two extremes (Schatz et al. 1999). The latter limit (B8) coincides with the Grad-Shafranov t=0 initial condition for degenerate, single-particle fluids, e.g. models B and C in Table 1 and Figure 3. The Grad-Shafranov

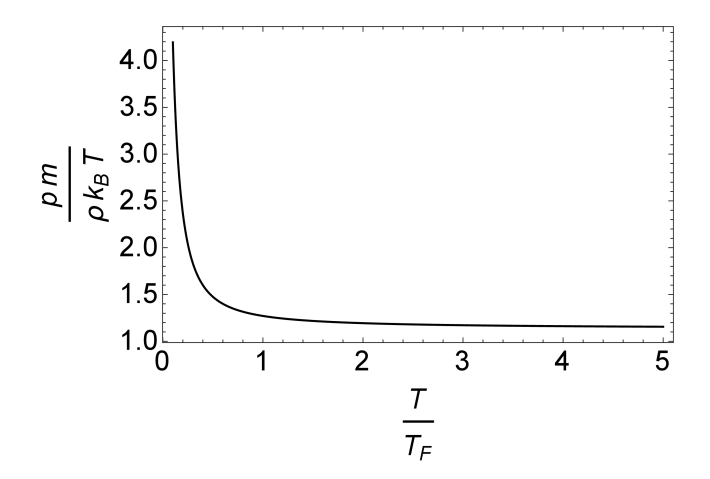


Figure B1. Thermal EOS for a nonrelativistic Fermi gas.

equilibria, calculated with (B8), adjust modestly, when thermal transport is switched on in PLUTO with (B7), suggesting that the equilibrium starting-point is broadly consistent with both (B7) and (B8), for the values of $\kappa_{||}$ and κ_{\perp} relevant here.

As noted throughout the body of the paper, it is the hot regions of the mountain where thermal conduction modifies the hydrodynamic structure the most as time passes. This is expected because the (dominant) parallel thermal conductivity $\kappa_{||}$ scales as $\kappa_{||} \propto T^{5/2}$ through (18). In hot regions, we have $T \gtrsim T_F$. Hence Fig. B1 implies a $\lesssim 20\%$ departure in $pm/\rho k_B T$ from the ideal gas law.

In Figure B2 we plot contours of $T_{\rm exact}/T_{\rm ideal}$ [i.e. $T_{\rm exact}$ from (B5) divided by $T_{\rm ideal}$ from (16)] (left panel) and $\kappa_{||,{\rm exact}}/\kappa_{||,{\rm ideal}}$ (similarly defined, right panel) for the realistic accreted crust model A with $M_a=1.8\times 10^{-5}M_{\odot}\approx 0.58M_c$ at t=0. We find $T_{\rm exact}/T_{\rm ideal}\gtrsim 0.85$ throughout the bulk of the mountain, i.e. the temperature is overestimated by $\lesssim 15\%$ in the densest regions of the mountain, where most mass resides, for this representative simulation. This translates into a $\lesssim 40\%$ overestimate in $\kappa_{||}\gg \kappa_{\perp}$ everywhere except at the mountain-atmosphere interface, where there is little mass, and the model breaks down anyway because of the artificial $\rho_{\rm atm}$.

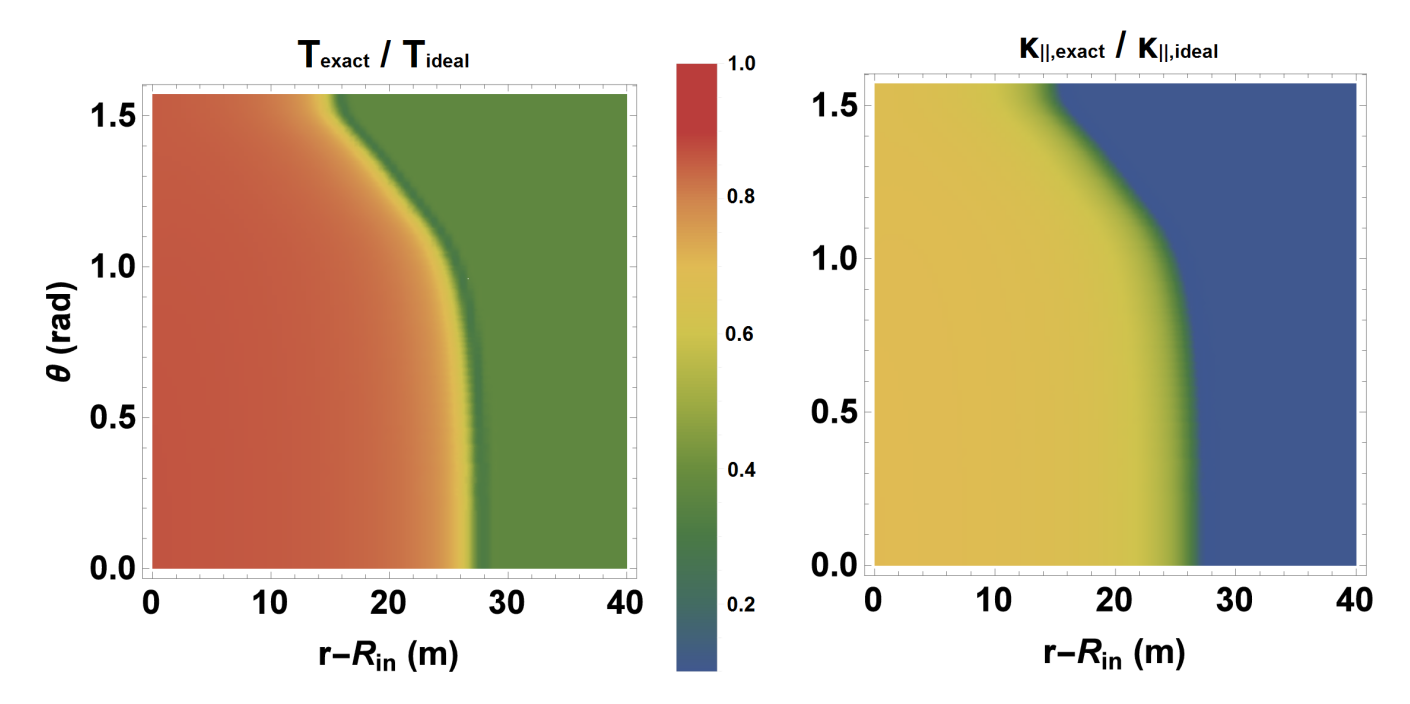


Figure B2. Contours of $T_{\rm exact}$ [computed using expression (B5)] normalised by $T_{\rm ideal}$ [computed using expression (16)] (left panel) and the similarly defined parallel conduction coefficients ratio $\kappa_{||,{\rm exact}}/\kappa_{||,{\rm ideal}}$ (right panel), plotted at t=0 for realistic crust model A with $M_a=1.8\times 10^{-5}M_{\odot}\approx 0.58M_c$. Red shades indicate values close to unity, while blue shades indicate values close to 0.1.